HECOLS Polish-French collaboration project

STRONGGRAVITY
EU FP7-SPACE research project 312789 2013 - 2017

The 7th FERO Meeting

FINDING EXTREME RELATIVISTIC OBJECTS

Krakow, 28th - 30th August 2014

Warm, soft corona above an accretion disk

In collaboration with:

**Julien Malzac, Bożena Czerny, Pierre-Olivier Petrucci,
Renaud Belmont**

Agata Różańska 29.08.2014, CAMK, Warsaw

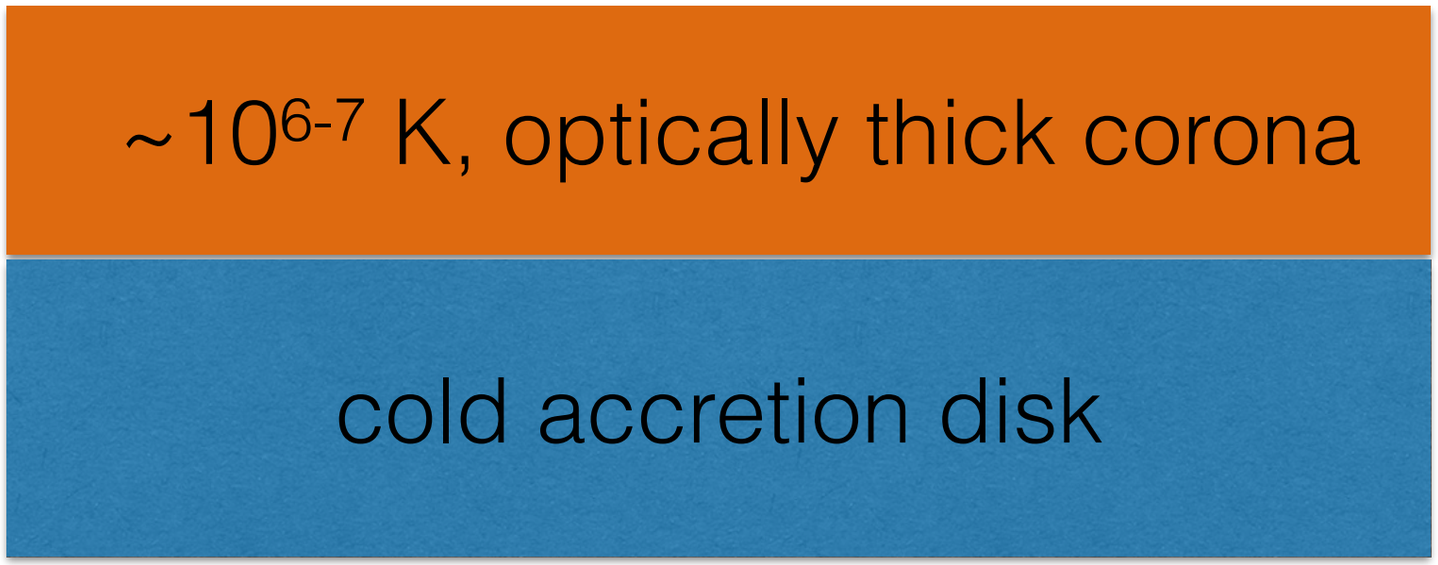

Warm, soft corona above an accretion disk

In collaboration with:

Julien Malzac, Bożena Czerny, Pierre-Olivier Petrucci, Renaud Belmont

Agata Różańska 29.08.2014, CAMK, Warsaw

International conference organised by Andrzej Zdziarski in 1996 in Koninki, Poland

International conference organised by Andrzej Zdziarski in 1996 in Koninki, Poland

- Power-law component with $\Gamma \sim 1.6 - 2.5^{1.5}$

  high energy cut off ~ 200 keV

  thermal source $T \sim 10^9 K$

- Compton reflection bump is produced by radiative interaction between hot and cold region

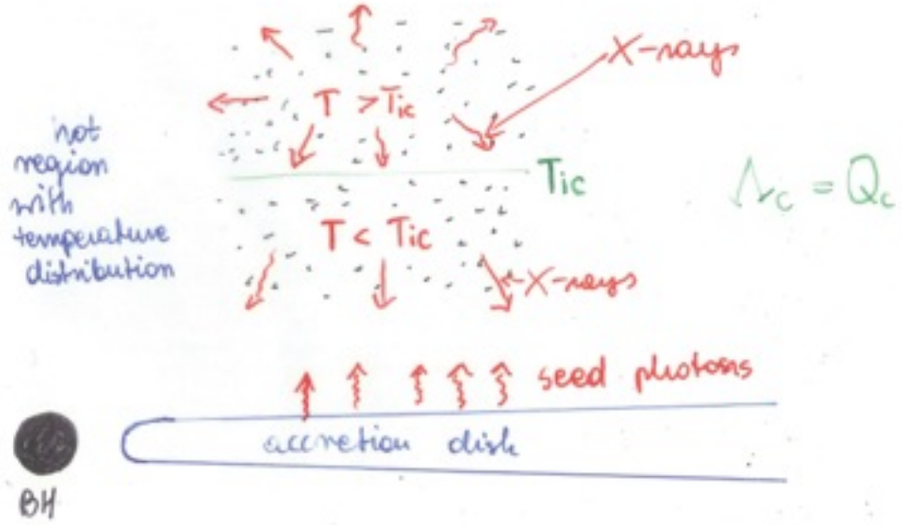

$A_c = Q_c$

For rare, hot plasma $T_{ic} \sim 10^8 K \Rightarrow$

1.) We need additional mechanism which heats plasma up ~ $10^9 K$

2) Feedback between X-rays and soft photons

International conference organised by Andrzej Zdziarski in 1996 in Koninki, Poland

- Power-law component with $\Gamma \sim 1.5 - 2.5$ / $1.6 - 2.5$

  high energy cut off ~200 keV

  thermal source $T \sim 10^9$ K

- Compton reflection bump is produced by radiative interaction between hot and cold region

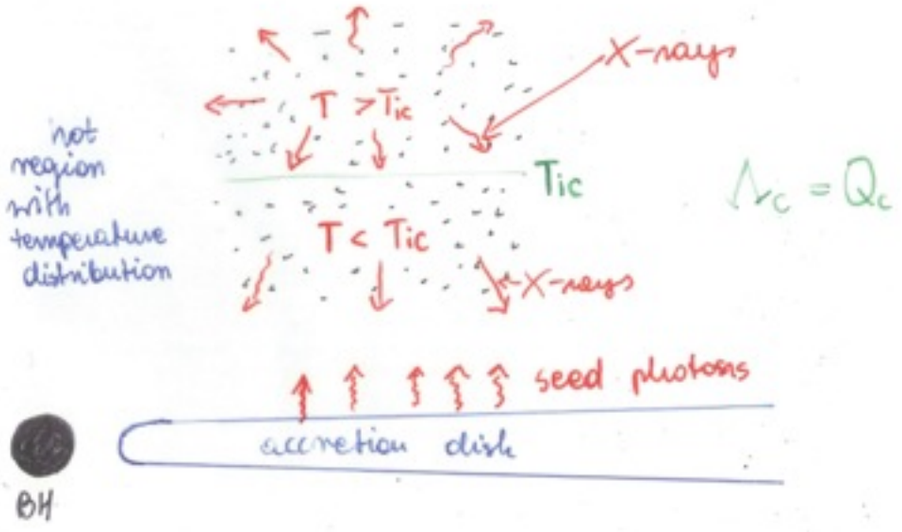

For rare, hot plasma $T_{ic} \sim 10^8$ K ⇒

1.) We need additional mechanism which heats plasma up ~ 10^9 K

2) Feedback between X-rays and soft photons

Variety of models which can be verified by observational features

Γ – photon index of X-ray spectrum

R – strength of Compton reflection bump

two groups depending on mechanism which heats plasma up to $T \sim 10^9$ K

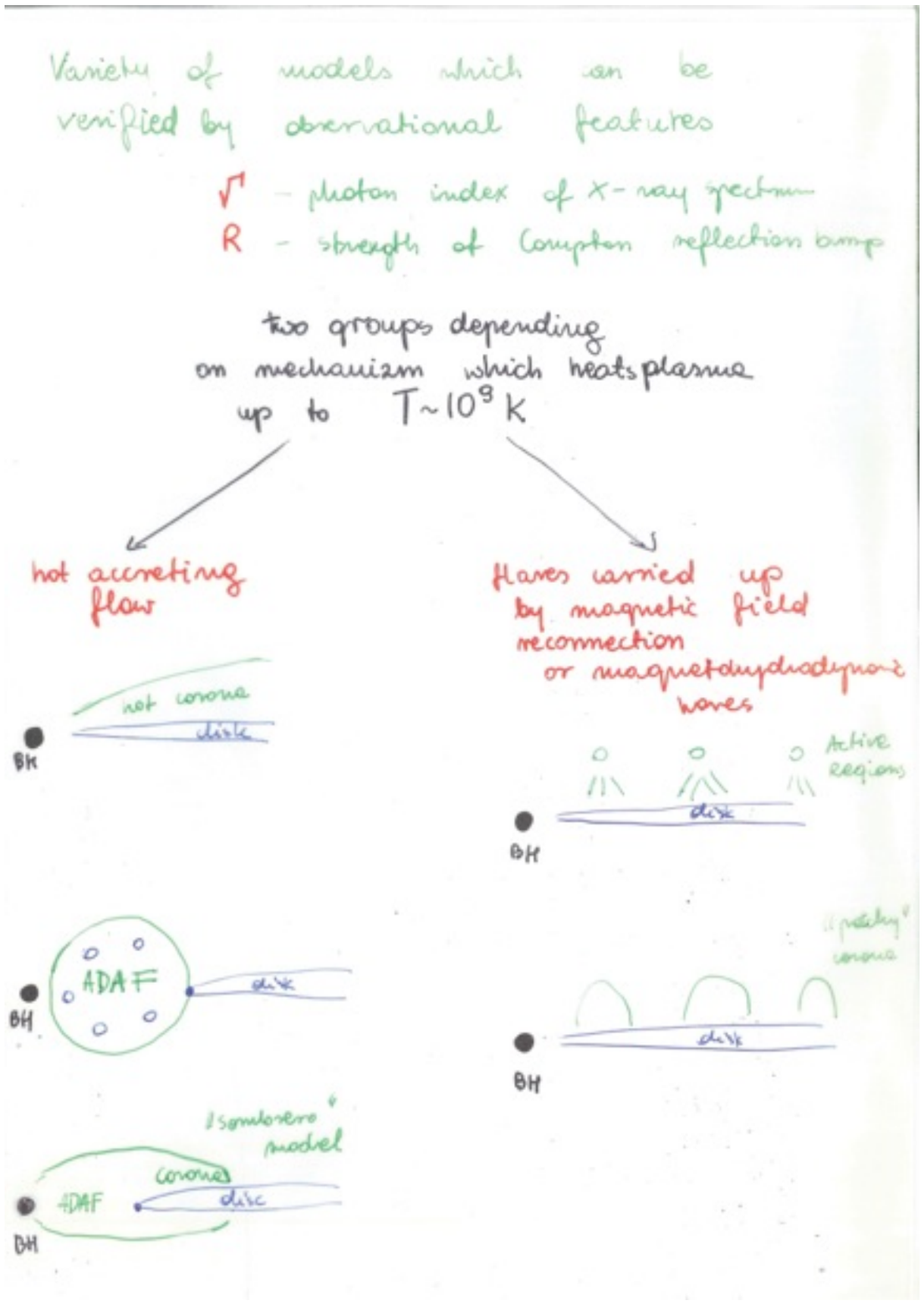

Hot corona 10^9 K, cooled by Comptonization was optically thin, as shown by Haardt Maraschi in 1993

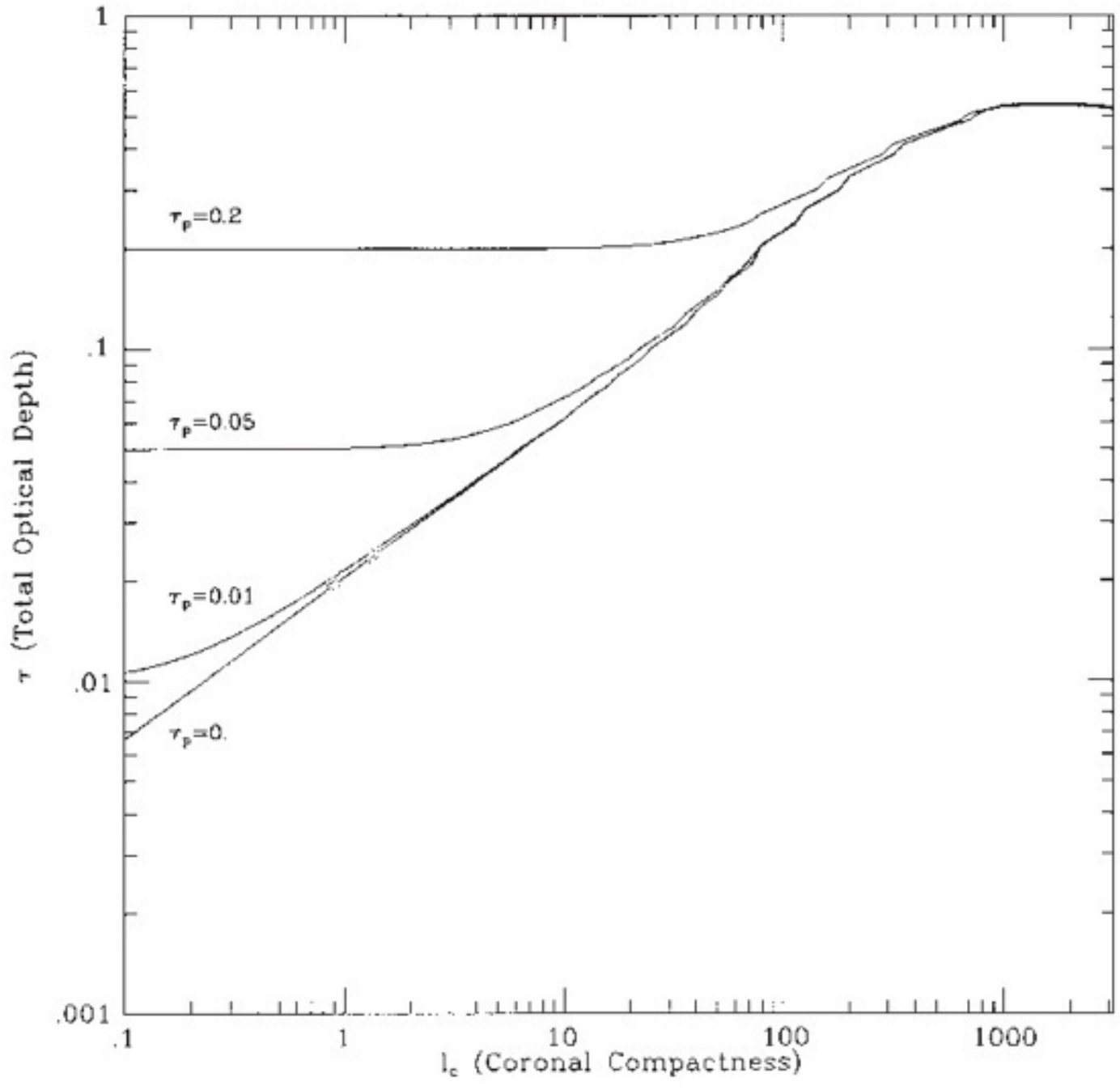

FIG. 3*a*

FIG. 3.—(*a*) Total optical depth τ as a function of the compactness l_c and the (*b*) Corresponding electron temperature according to the energy balance equation.

Continuum energy distribution in radio-quiet AGN:

Magdziarz et al. 1998
NGC 5548 Sy1
HST, IUE, Rosat, Ginga, OSSE

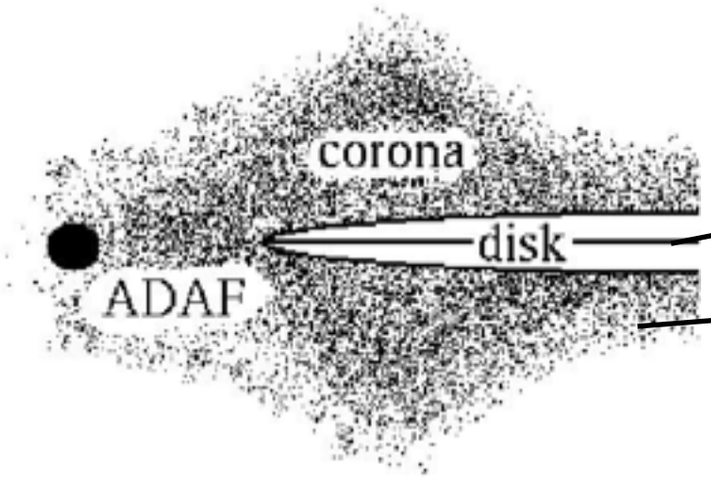

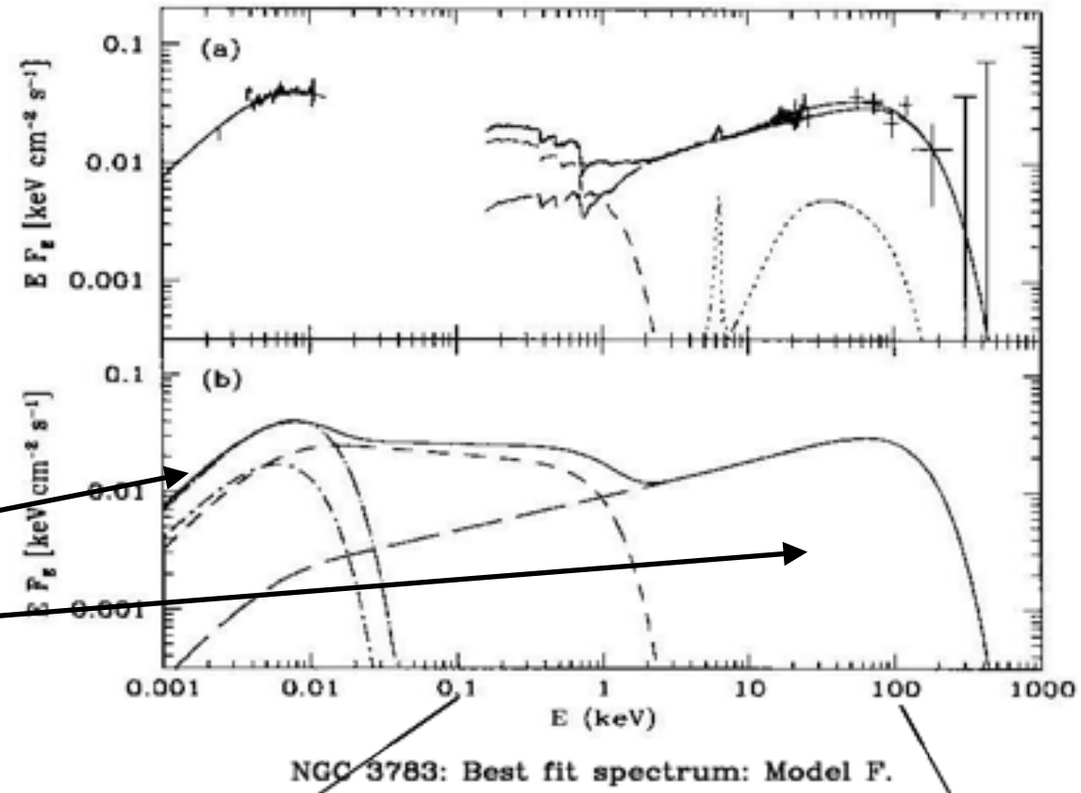

De Rosa et al. 2002
NGC 3783 Sy1

Broad-band spectrum
Beppo-SAX

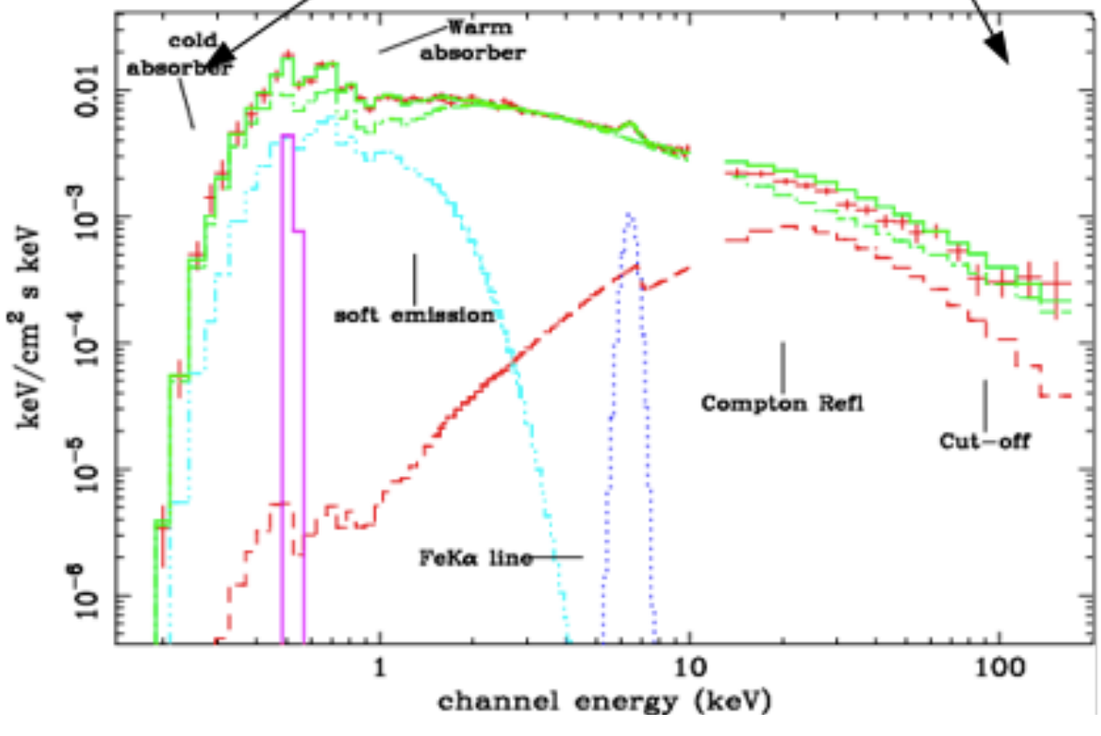

Continuum energy distribution in radio-quiet AGN:

Radiative interaction of hard X-rays with colder disk matter:

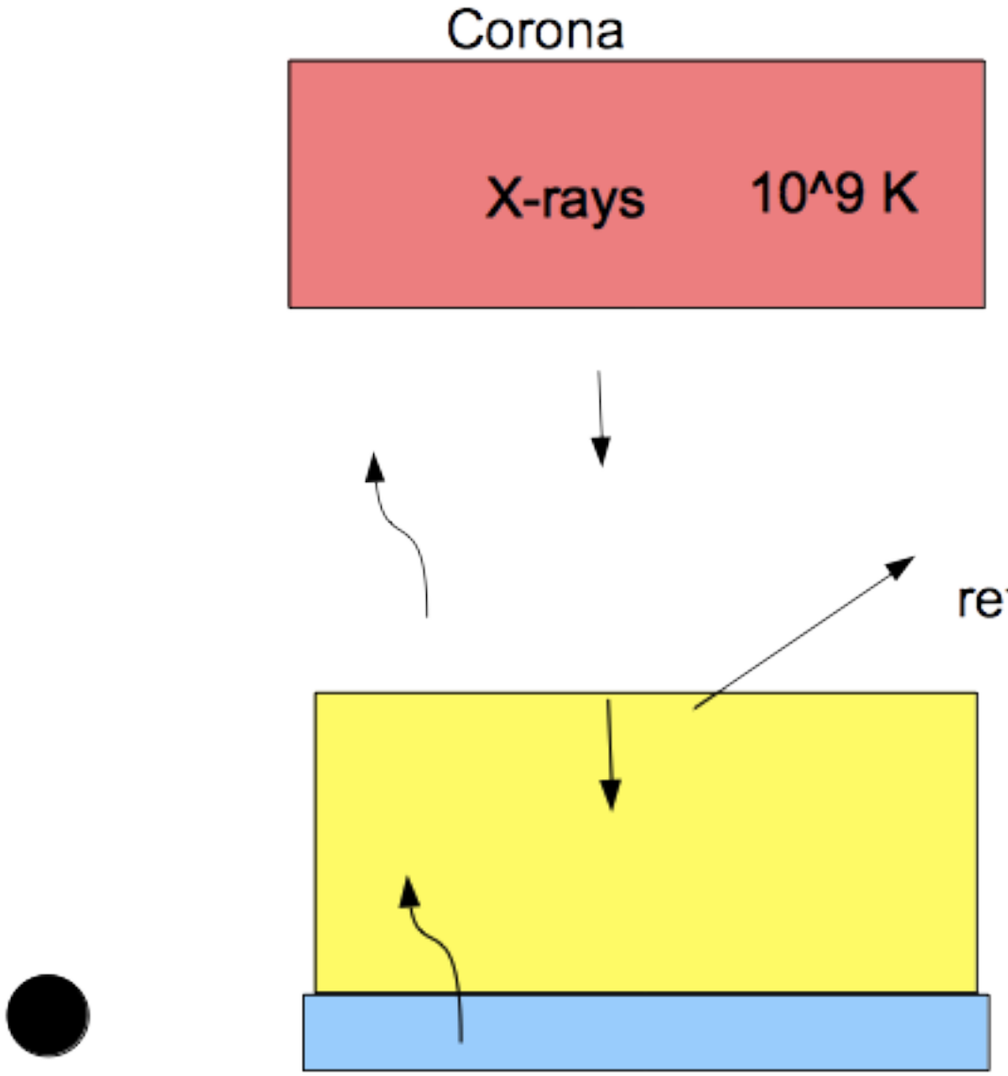

$$F_X = f_{cor} * \frac{3 G M \dot{M}}{8 \pi r^3} * b(r)$$

$$F_{disk} = (1 - f_{cor}) * \frac{3 G M \dot{M}}{8 \pi r^3} * b(r)$$

The transition layer between an accretion disk and corona:

Nayakshin et al. 2000

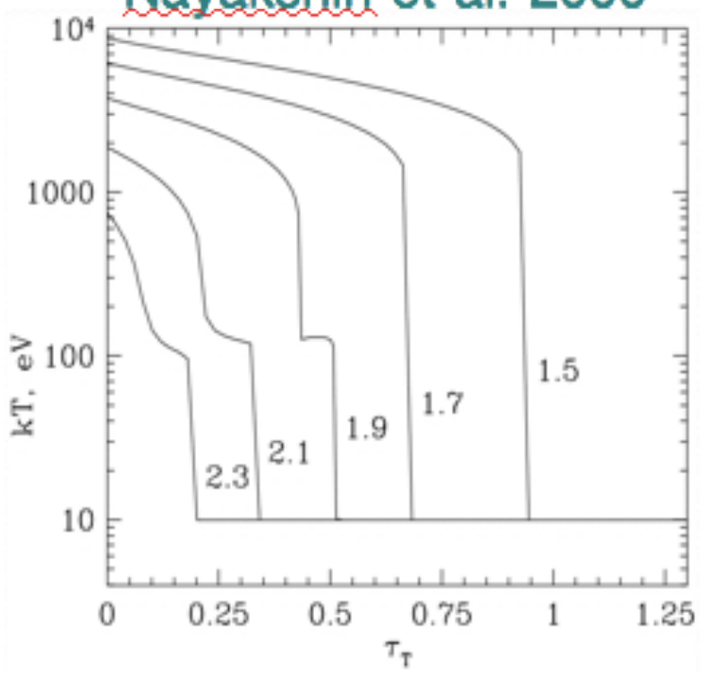

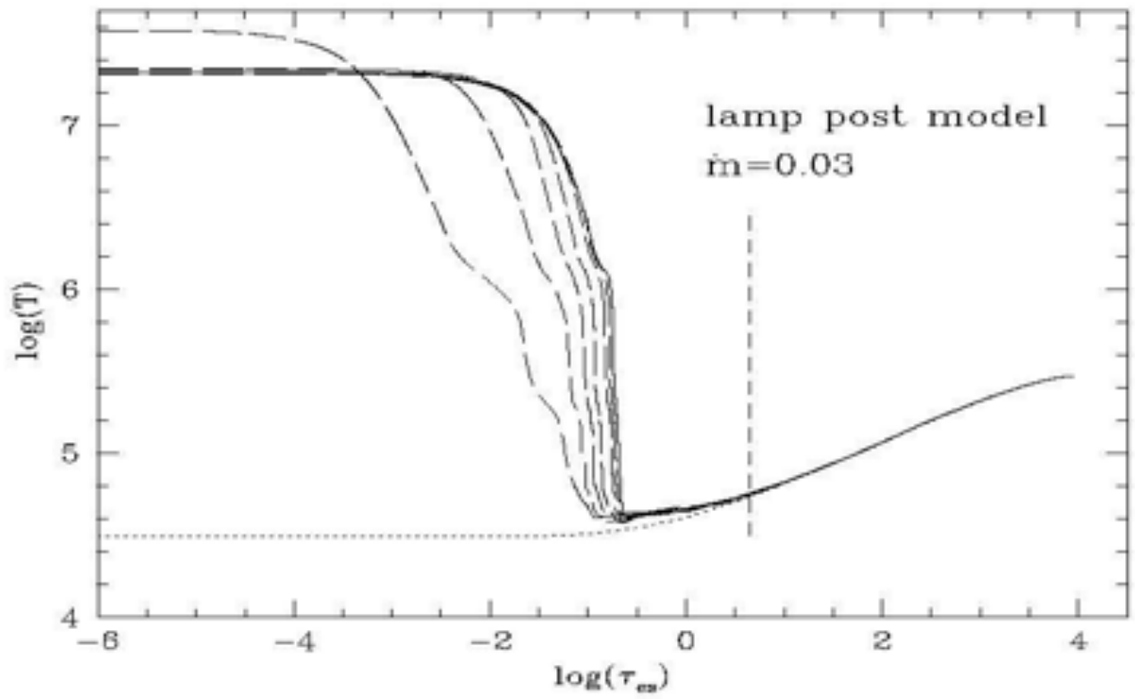

Ballantyne et al. 2001

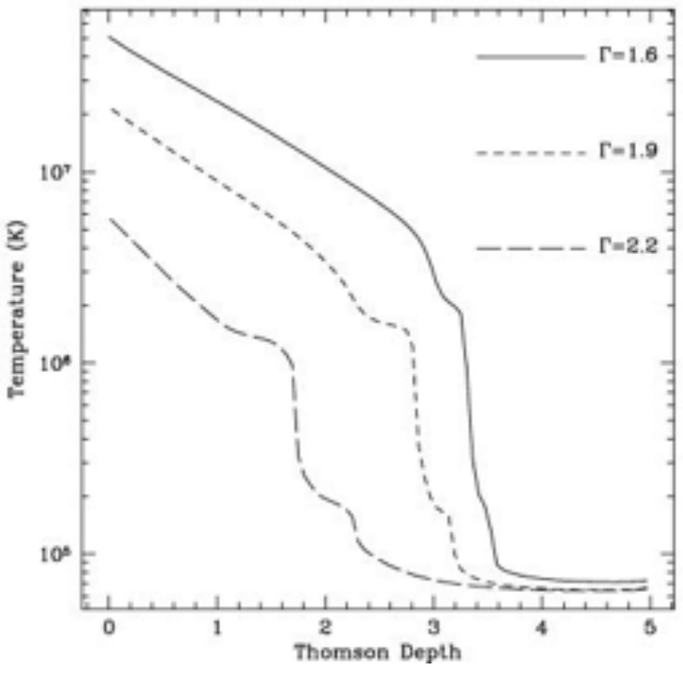

TITAN , Różańska et al 2002

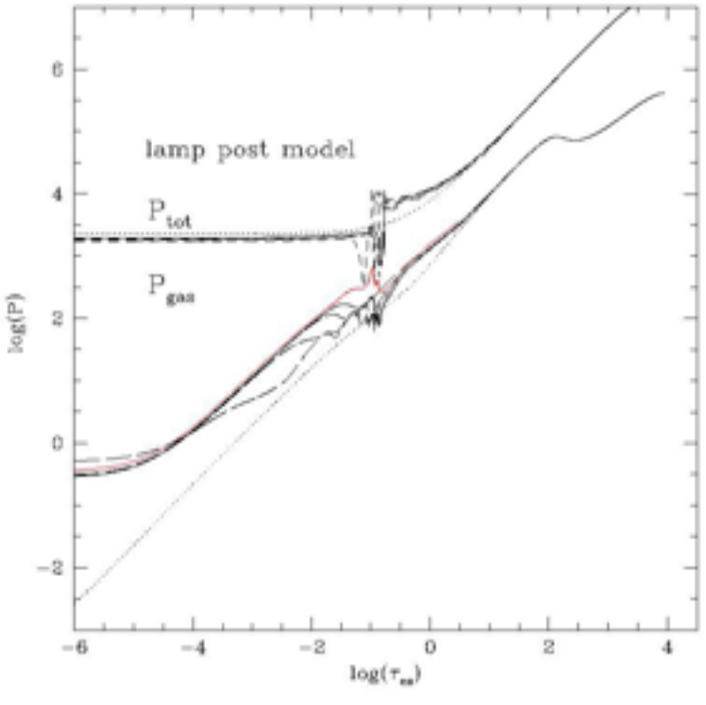

The transition layer between an accretion disk and corona:

Comparing of work by: Nayakshin, Ballantyne and **TITAN** :

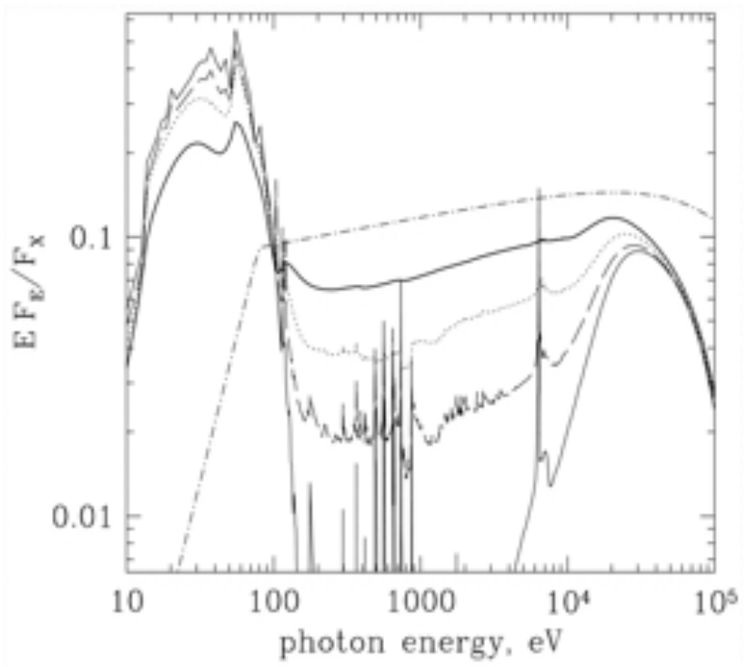

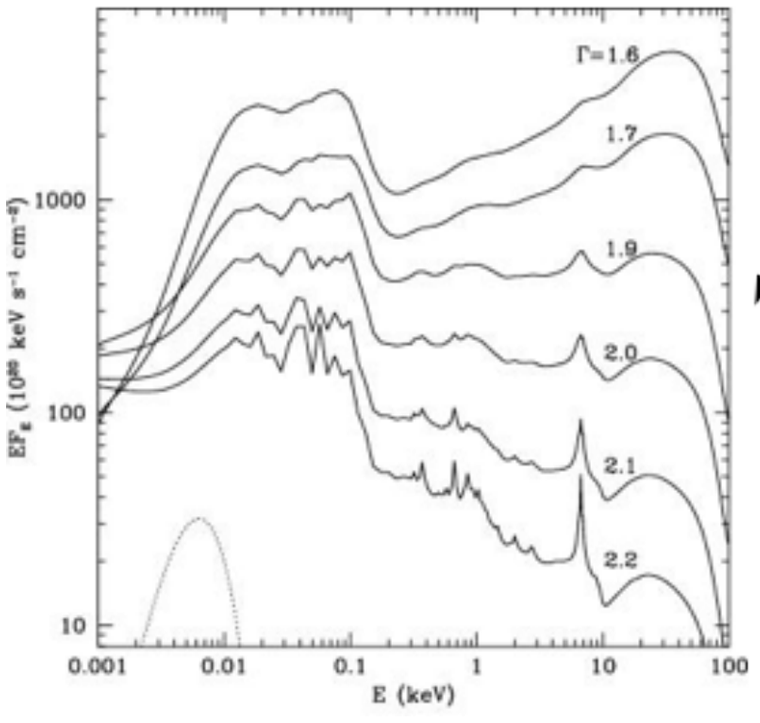

non-LTE,
external illumination
900 atomic
bound-bound
transitions.

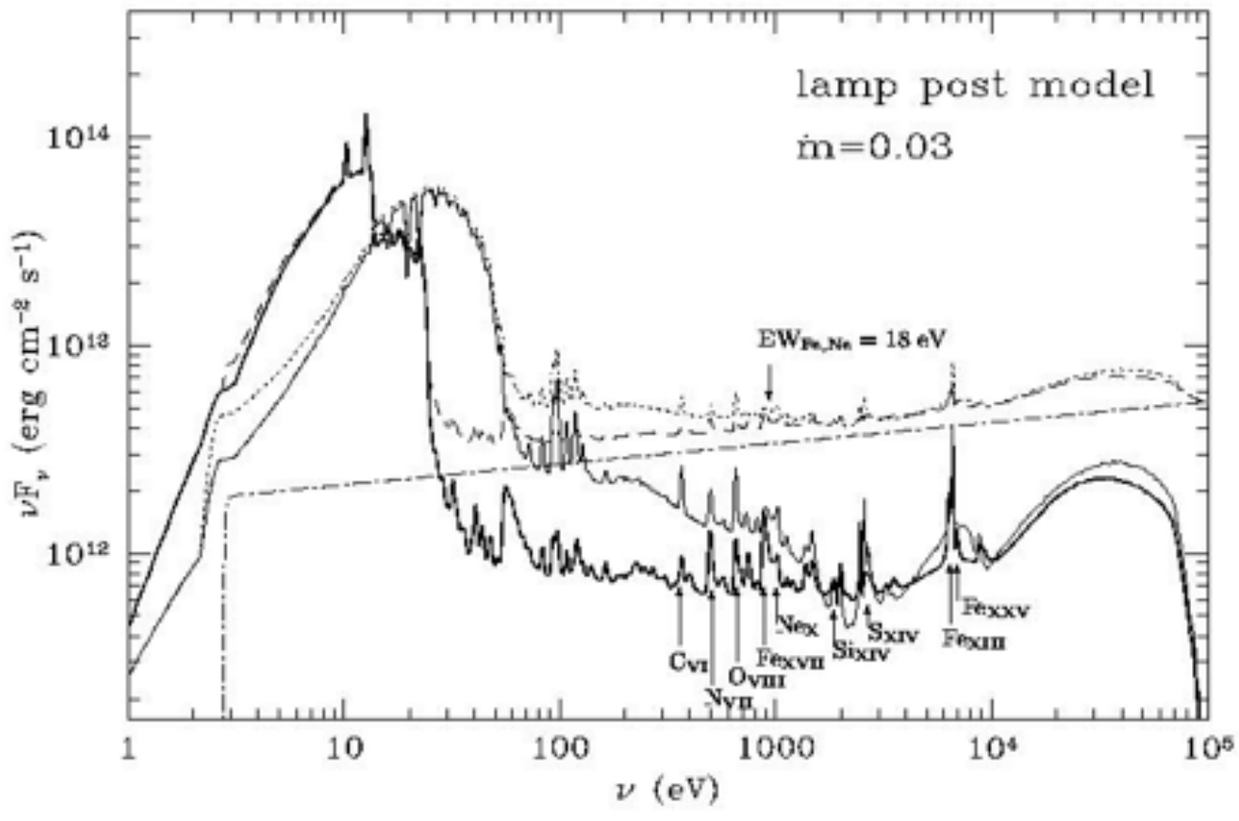

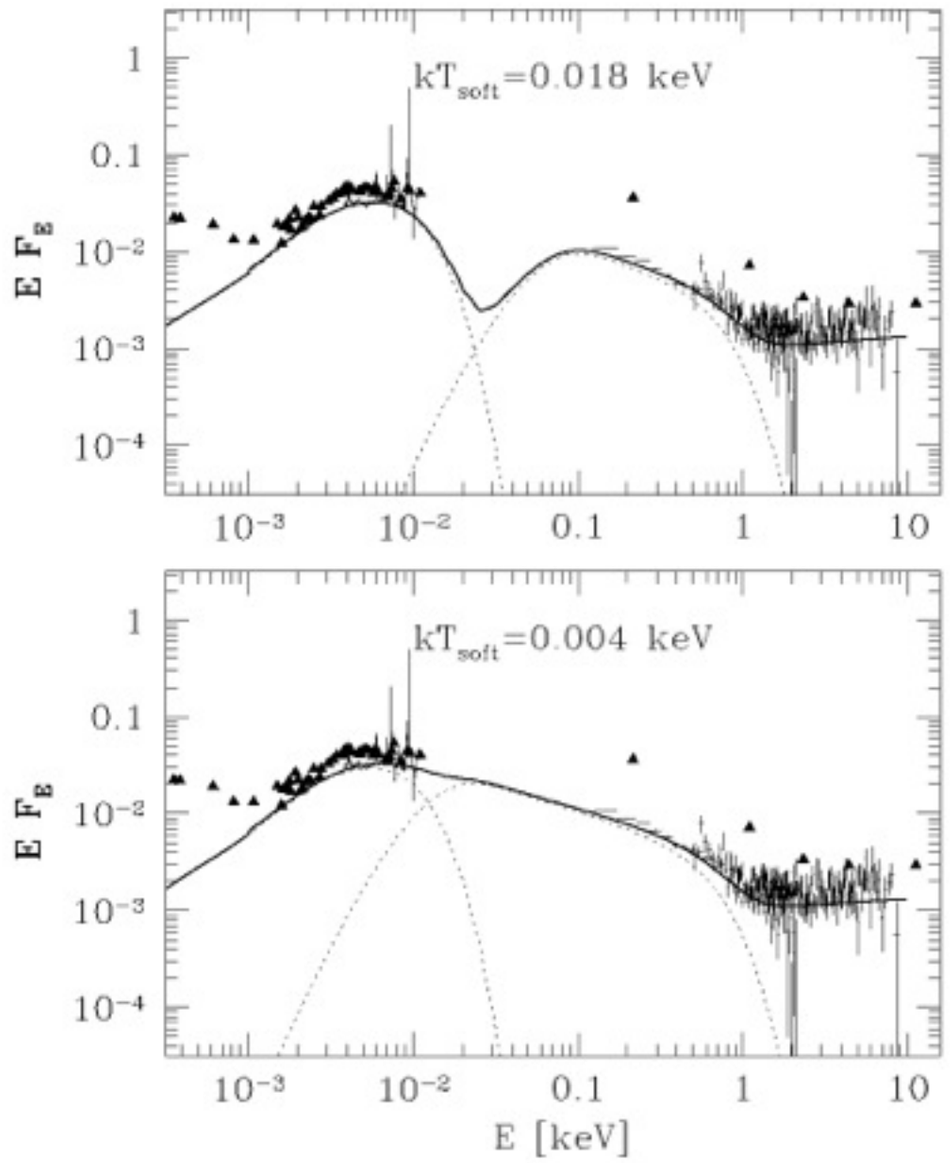

FIG. 9.—Broadband spectrum of PG 1211 + 143 in the IR–X range. In the lower panel we show the model calculated assuming that the accretion disk provides seed photons for Comptonization by the hot plasma. In the upper panel we show the model which assumes that the soft photons are emitted in the hotter plasma. The solid triangles are data points from Elvis et al. (1994). The UV spectrum with emission lines are the *HST* data (Bechtold et al. 2000) and the crosses are the X-ray data from *ASCA* and *ROSAT*. The Comptonized disk model was fitted to the X-ray data. In both cases, absorption in soft X-rays is neglected in the plot, and for the modeling purposes, the X-ray data were corrected for absorption. Optical/UV spectrum was modeled with a standard disk. Thick solid line is the sum of all model components.

Janiuk et al. 2001 PG1211+143

Janiuk et al. 2001 PG1211+143

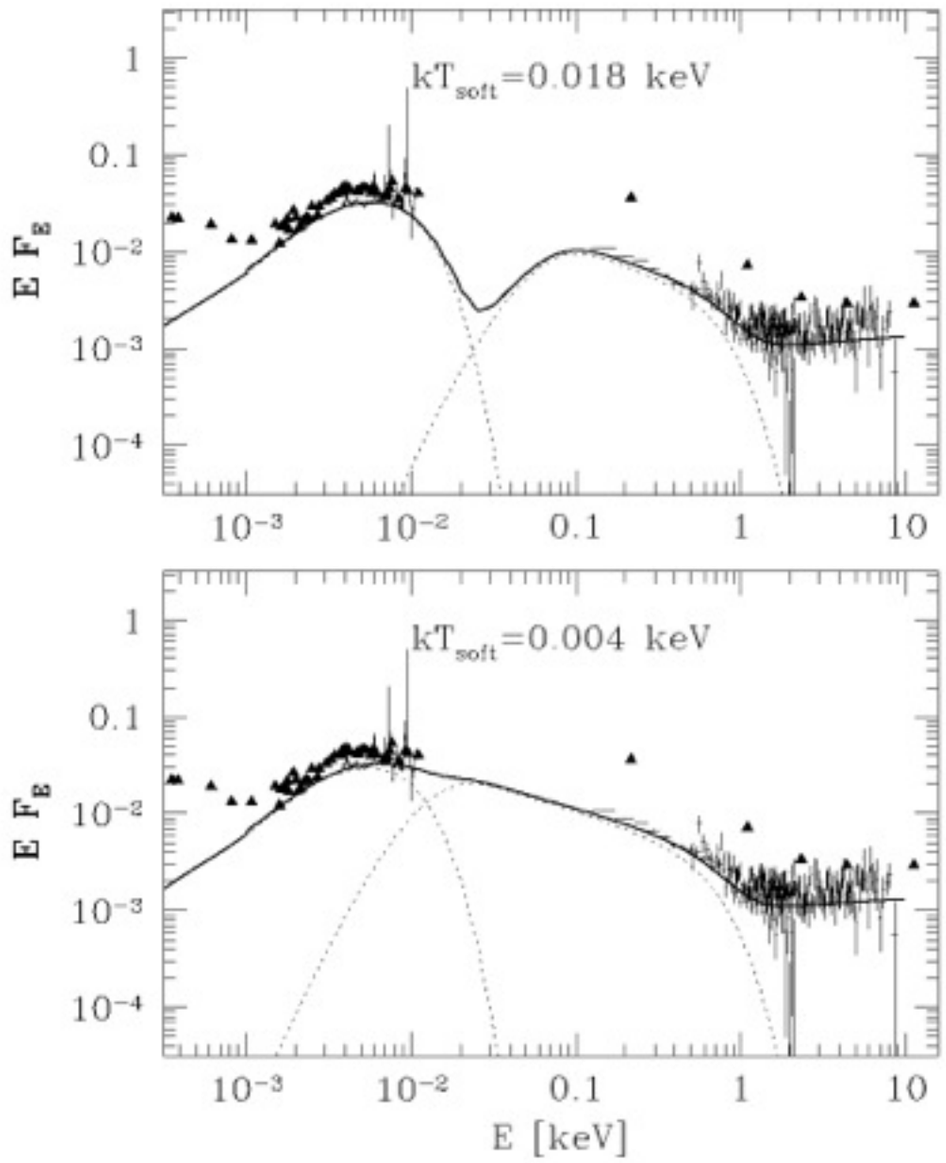

FIG. 9.—Broadband spectrum of PG 1211+143 in the IR–X range. In the lower panel we show the model calculated assuming that the accretion disk provides seed photons for Comptonization by the hot plasma. In the upper panel we show the model which assumes that the soft photons are emitted in the hotter plasma. The solid triangles are data points from Elvis et al. (1994). The UV spectrum with emission lines are the *HST* data (Bechtold et al. 2000) and the crosses are the X-ray data from *ASCA* and *ROSAT*. The Comptonized disk model was fitted to the X-ray data. In both cases, absorption in soft X-rays is neglected in the plot, and for the modeling purposes, the X-ray data were corrected for absorption. Optical/UV spectrum was modeled with a standard disk. Thick solid line is the sum of all model components.

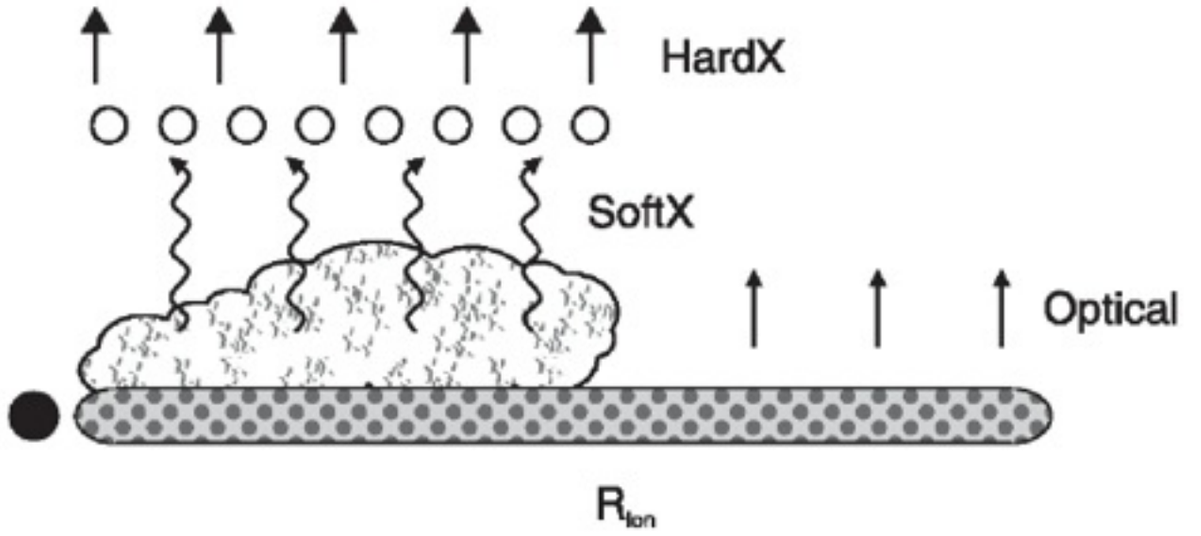

FIG. 10.—Geometry of the accretion flow in PG 1211+143 consistent with the spectral model presented in Fig. 9. The optical flux is emitted by the cold accretion disk ($T \sim 10^4$ K). The disk is the source of seed photons for the hot Comptonizing cloud ($T \sim 10^6$ K, $\tau \sim 20$), which extends below the transition radius R_{ion}. The hard X-ray flux is emitted by the hot flare region ($T \sim 10^9$ K) and are partially reflected by the cloud ($\xi \sim 500$, $\Omega/2\pi \sim 1$).

large optical depth

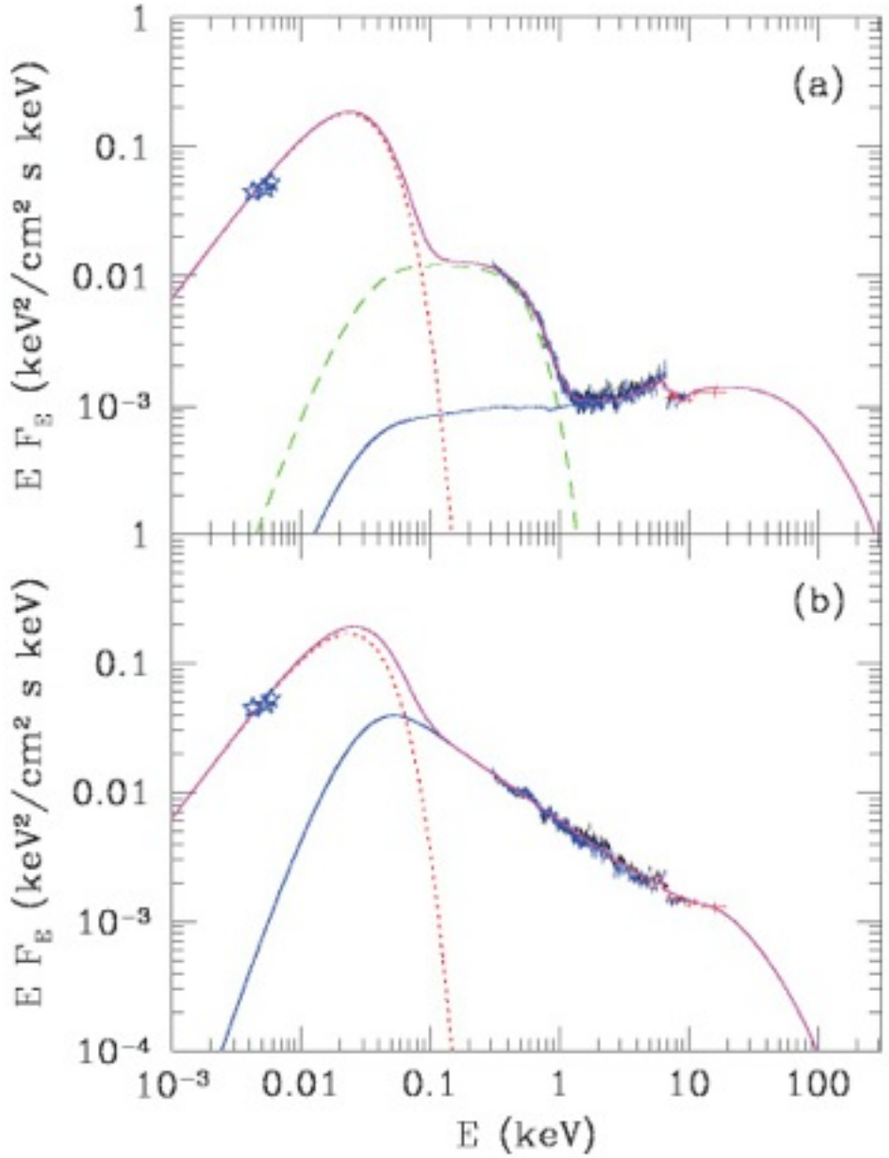

Figure 3. Unabsorbed model components together with unfolded and unabsorbed data from PG 1211+143. Open stars represent OM data, crosses (black, blue and red in the online version) represent EPIC MOS, PN and (non-simultaneous) *RXTE* PCA data, respectively. The dotted curve (red in the online version) represents the disc spectrum. (a) The model with two Comptonized components and ionized reflection. In this model the soft excess comes from Comptonization in warm optically thick plasma (dashed curve, green in the online version). (b) The model with complex ionized, relativistically smeared absorption, which is not seen here as this is *unabsorbed* model. Instead, the intrinsic spectrum is very different and does not require any additional component to explain the soft excess. In this interpretation the soft excess is due solely to complex absorption. This figure can be seen in colour in the on-line version of this article on *Synergy*.

Gierliński & Done 2004

Gierliński & Done 2004

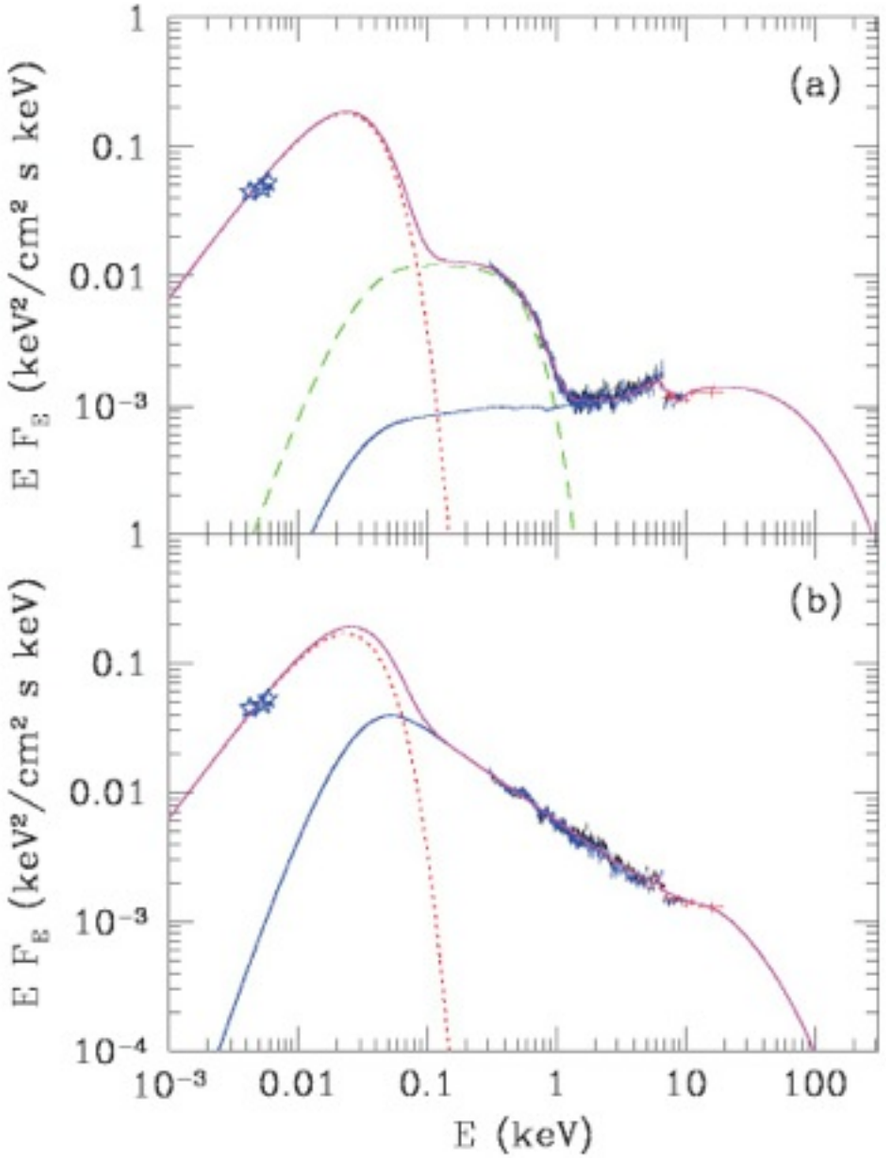

Figure 3. Unabsorbed model components together with unfolded and unabsorbed data from PG 1211+143. Open stars represent OM data, crosses (black, blue and red in the online version) represent EPIC MOS, PN and (non-simultaneous) *RXTE* PCA data, respectively. The dotted curve (red in the online version) represents the disc spectrum. (a) The model with two Comptonized components and ionized reflection. In this model the soft excess comes from Comptonization in warm optically thick plasma (dashed curve, green in the online version). (b) The model with complex ionized, relativistically smeared absorption, which is not seen here as this is *unabsorbed* model. Instead, the intrinsic spectrum is very different and does not require any additional component to explain the soft excess. In this interpretation the soft excess is due solely to complex absorption. This figure can be seen in colour in the on-line version of this article on *Synergy*.

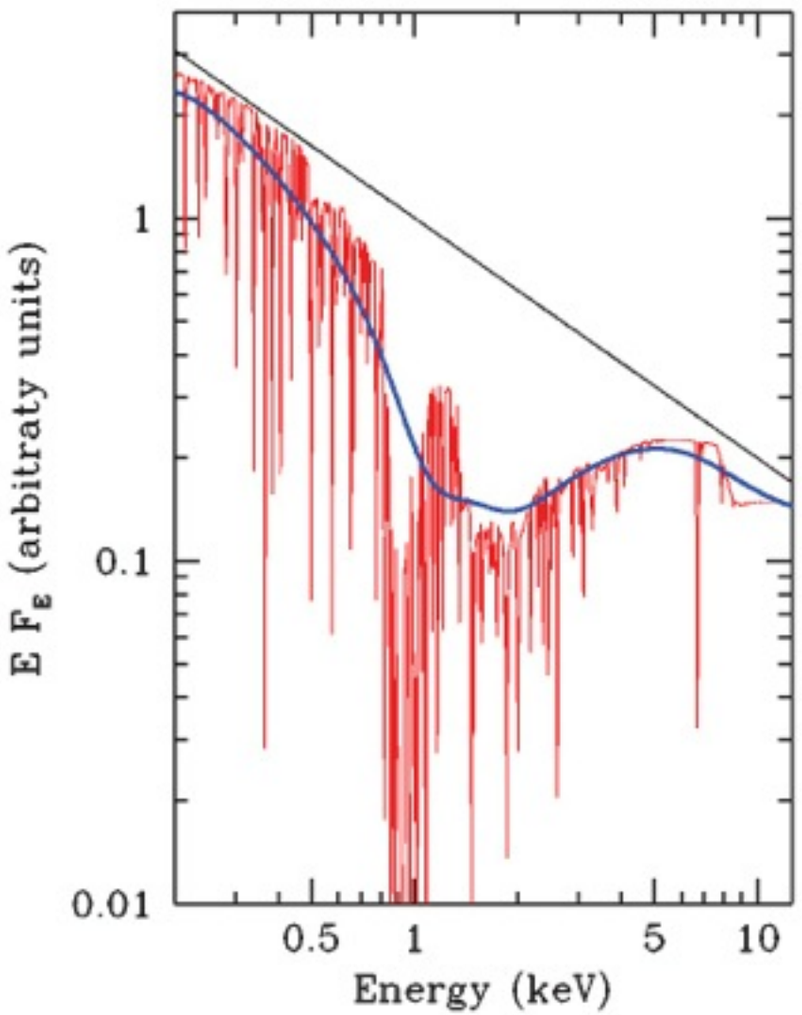

Figure 2. An illustration of the ionized absorption model creating the soft excess. The upper line is an underlying power law with spectral index $\Gamma = 2.7$. The grey line (red in the online version) shows the multiple absorption features predicted by an XSTAR model with $N_{\rm H} = 33 \times 10^{22}$ cm^{-2} and $\xi = 460$ erg cm s^{-1} (best-fitting parameters to PG 1211+143). The curved thick line shows the this absorbed continuum convolved with a Gaussian of $\sigma/E = 0.28$. This figure can be seen in colour in the on-line version of this article on *Synergy*.

Jin, Ward, Done, Gelbord 2012

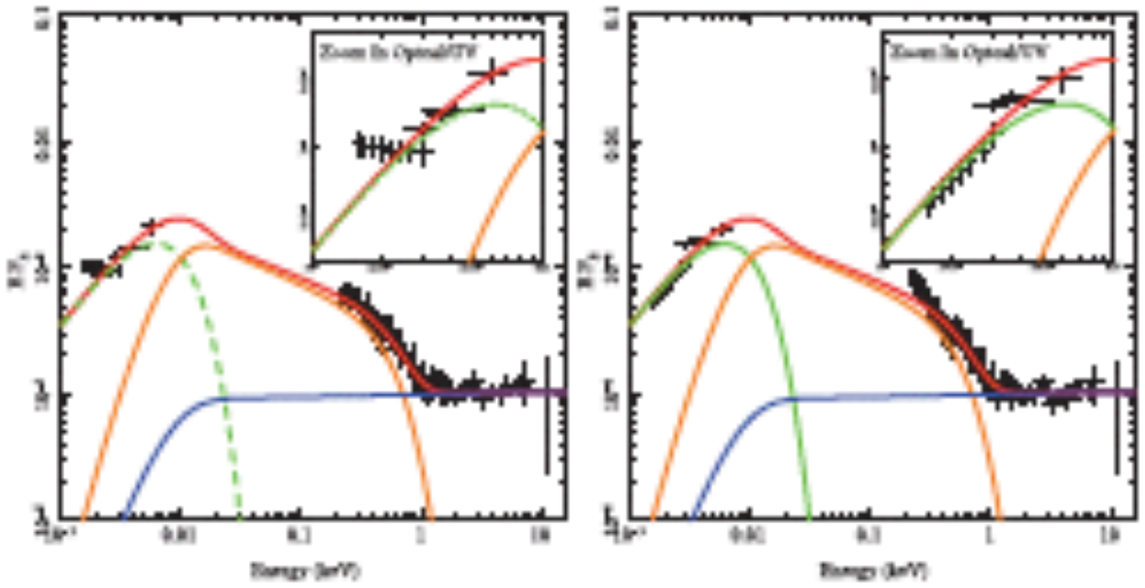

d)

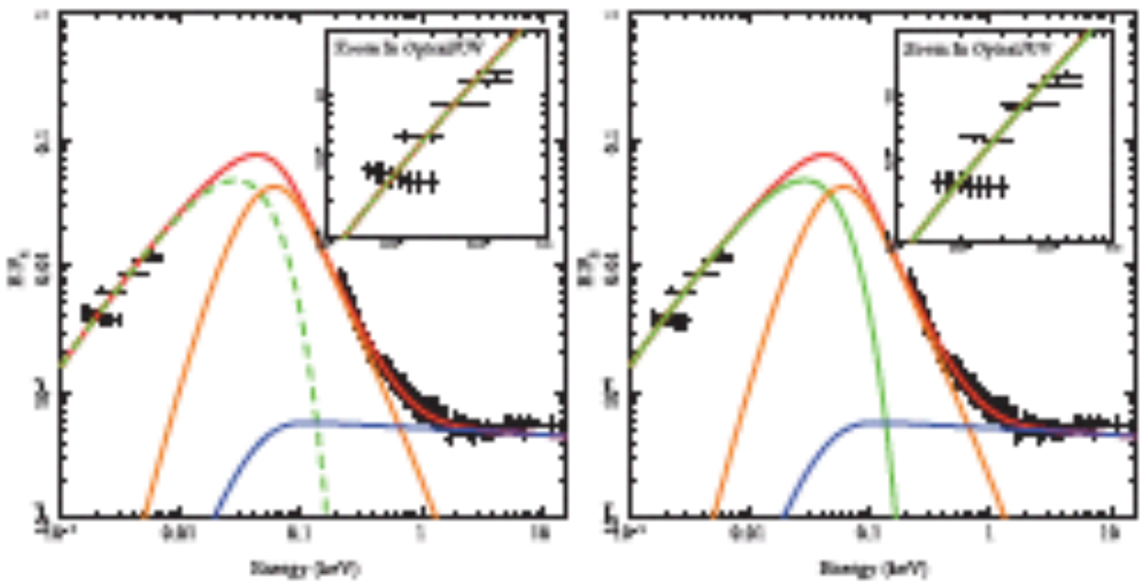

Jin, Ward, Done, Gelbord 2012

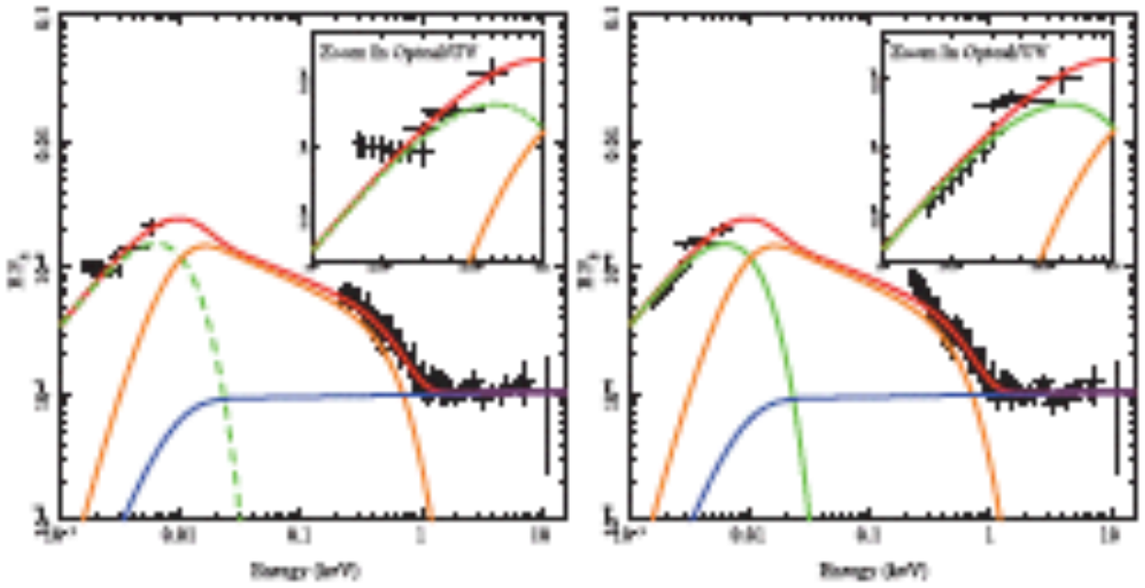

d)

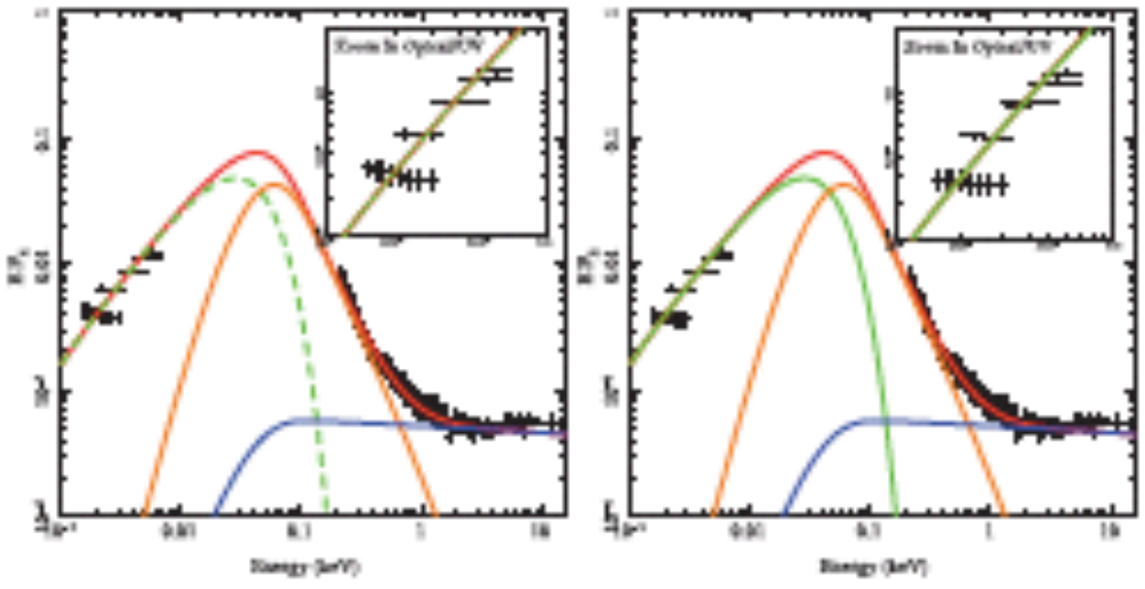

ID	Common Name[a]	Redshift	2XMMi catalogue IAU name (2XMM[b])	*XMM–Newton* Observation date
1	UM 269	0.308	J004319.7+005115	2002-01-04
2	Mrk 1018	0.043	J020615.9−001730	2005-01-15
3	NVSS J030639	0.107	J030639.5+000343	2003-02-11
4	2XMMiDR7	0.145	J074601.2+280732	2001-04-26
5	2XMMiDR7	0.358	J080608.0+244421	2001-10-26
6	HS 0810+5157	0.377	J081422.1+514839	2003-04-27
7	RBS 0769	0.160	J092246.9+512037	2005-10-08
8	RBS 0770	0.033	J092342.9+225433*	2006-04-18
9	Mrk 0110	0.035	J092512.8+521711	2004-11-15
10	PG 0947+396	0.206	J095048.3+392650	2001-11-03
11	2XMMiDR7	0.373	J100025.2+015852	2003-12-10
12	2XMMiDR7	0.206	J100523.9+410746	2004-04-20
13	PG 1004+130	0.241	J100726.0+124856	2003-05-04
14	RBS 0875	0.178	J103059.0+310255	2000-12-06
15	KUG 1031+398	0.043	J103438.6+393828	2002-05-01
16	PG 1048+342	0.160	J105143.8+335927	2002-05-13
17	1RXS J111007	0.262	J111006.8+612522*	2006-11-25
18	PG 1115+407	0.155	J111830.2+402554	2002-05-17
19	2XMMiDR7	0.101	J112328.0+052823	2001-12-15
20	RX J1140.1+0307	0.081	J114008.7+030710	2005-12-03
21	PG 1202+281	0.165	J120442.1+275412	2002-05-30
22	1AXG J121359+1404	0.154	J121356.1+140431	2001-06-15
23	2E 1216+0700	0.080	J121930.9+064334	2002-12-18
24	1RXS J122019	0.286	J122018.4+064120	2002-07-05
25	LBQS 1228+1116	0.236	J123054.1+110011	2005-12-17
26	2XMMiDR7	0.304	J123126.4+105111	2005-12-17
27	Mrk 0771	0.064	J123203.6+200929	2005-07-09
28	RX J1233.9+0747	0.371	J123356.1+074755	2004-06-05
29	RX J1236.0+2641	0.209	J123604.0+264135*	2006-06-24
30	PG 1244+026	0.048	J124635.3+022209	2001-06-17
31	2XMMiDR7	0.316	J125553.0+272405	2000-06-21
32	RBS 1201	0.091	J130022.1+282402	2004-06-06
33	2XMMiDR7	0.334	J132101.4+340658	2001-01-09
34	1RXS J132447	0.306	J132447.6+032431	2004-01-25
35	UM 602	0.237	J134113.9−005314	2005-06-28
36	1E 1346+26.7	0.059	J134834.9+263109	2000-06-26
37	PG 1352+183	0.151	J135435.6+180518	2002-07-20
38	Mrk 0464	0.050	J135553.4+383428	2002-12-10
39	1RXS J135724	0.106	J135724.5+652506	2005-04-04
40	PG 1415+451	0.114	J141700.7+445606	2002-12-08
41	PG 1427+480	0.221	J142943.0+474726	2002-05-31
42	NGC 5683	0.037	J143452.4+483943	2002-12-09
43	RBS 1423	0.208	J144414.6+063306	2005-02-11
44	PG 1448+273	0.065	J145108.7+270926	2003-02-08
45	PG 1512+370	0.371	J151443.0+365050	2002-08-25
46	Q 1529+050	0.218	J153228.8+045358	2001-08-21
47	1E 1556+27.4	0.090	J155829.4+271715	2002-09-10
48	Mrk 0493	0.031	J155909.6+350147	2003-01-16
49	II Zw 177	0.081	J221918.5+120753	2001-06-07
50	PG 2233+134	0.326	J223607.6+134355	2003-05-28
51	Mrk 0926	0.047	J230443.3−084111	2000-12-01

Jin, Ward, Done, Gelbord 2012

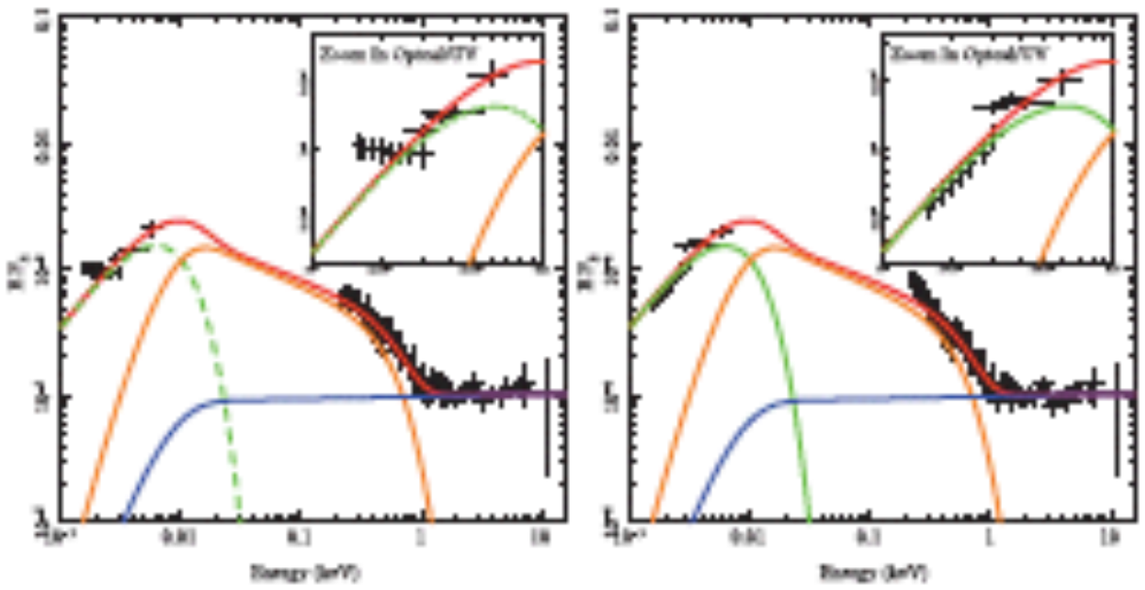

d)

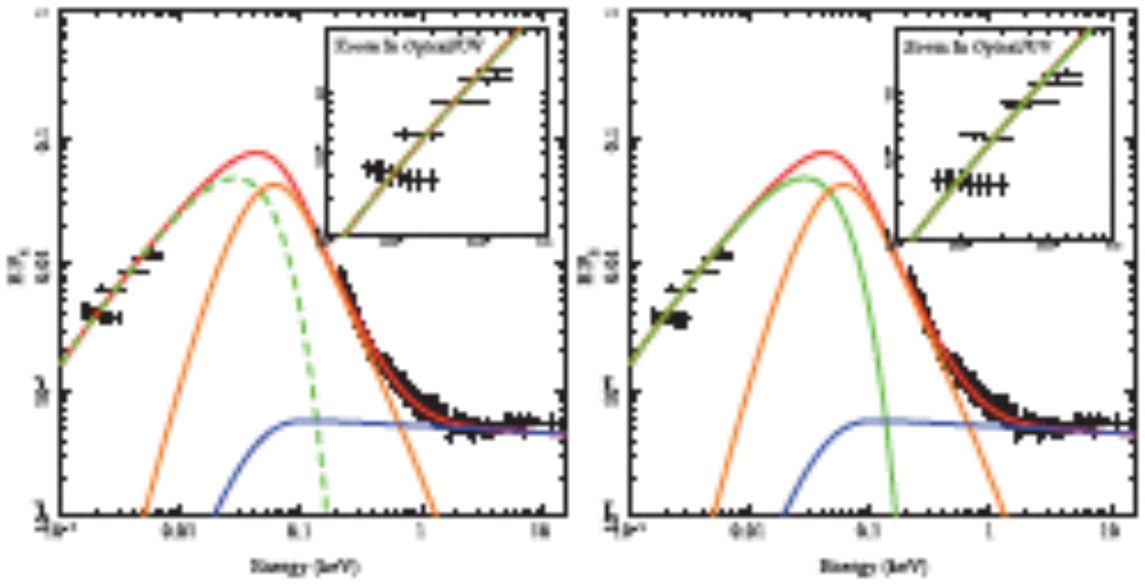

ID	$N_{H,gal}$ ($\times10^{20}$)	$N_{H,int}$ ($\times10^{20}$)	Γ_{pow}	f_{pl}	R_{cor} (r_g)	T_e (keV)	τ
1	1.79	0.00	1.71	0.69	100.	0.262	17.2
2	2.43	1.06	1.77	0.39	100.	0.226	15.7
3	6.31	9.88	1.91	0.25	11.9	0.108	20.0
4	3.49	2.81	1.66	0.50	100.	0.312	15.4
5	3.53	4.03	2.12	0.36	54.9	0.205	14.9
6	4.24	0.00	1.93	0.46	23.9	0.347	12.6
7	1.33	3.74	2.20*	0.29	8.37	0.137	40.3
8	3.12	7.35	1.82	0.15	24.1	1.380	3.44
9	1.30	1.36	1.71	0.71	12.9	0.360	11.1
10	1.74	0.00	1.91	0.32	100.	0.295	13.8
11	1.72	2.00	1.71	0.49	20.2	0.449	9.23
12	1.20	1.08	1.68	0.48	20.6	0.402	11.4
13	3.56	0.00	1.37	0.87	10.9	0.146	17.9
14	1.76	0.00	1.72	0.71	100.	0.294	16.0
15	1.31	2.43	2.20*	0.09	14.2	0.214	12.3
16	1.70	0.65	1.72	0.31	100.	0.327	13.0
17	0.65	0.85	1.74	0.14	48.7	0.326	11.4
18	1.45	0.19	2.20*	0.24	29.5	0.254	13.6
19	3.70	1.41	1.98	0.19	45.8	0.142	21.5
20	1.91	4.77	2.20*	0.36	9.63	0.210	16.8
21	1.77	0.00	1.79	0.75	22.7	0.206	19.6
22	2.75	8.84	1.86	0.21	50.5	0.108	25.1
23	1.59	0.00	1.41	0.45	86.9	0.626	9.59
24	1.63	0.00	1.82	0.94	32.2	0.182	32.2
25	2.34	0.00	1.79	0.40	25.7	0.351	12.9
26	2.31	7.25	2.10	0.03	33.8	0.310	9.69
27	2.75	0.00	1.85	0.22	37.6	0.554	8.29
28	1.45	0.00	1.69	0.60	71.3	0.353	13.7
29	1.18	1.36	2.00	0.12	30.9	0.389	8.85
30	1.87	2.64	2.20*	0.36	9.67	0.234	16.9
31	0.84	0.00	1.68	0.54	100.	0.404	12.9
32	0.90	0.14	1.80	0.44	100.	0.388	12.2
33	1.07	0.82	2.18	0.57	15.0	0.226	15.6
34	1.83	0.93	1.90	0.33	100.	0.252	14.8
35	1.76	0.90	1.80	0.83	100.	0.202	20.4
36	1.18	3.94	2.18	0.22	16.2	2.000	2.71
37	1.82	0.00	2.04	0.38	100.	0.219	17.2
38	1.42	0.37	1.58	0.97	100.	0.251	25.0
39	1.36	4.77	2.10	0.11	40.6	0.281	11.4
40	0.77	5.21	2.05	0.06	24.0	0.930	4.28
41	1.81	0.00	1.90	0.39	28.9	0.298	14.0
42	2.86	3.29	1.84	0.41	100.	0.083	31.3
43	2.69	0.00	1.71	0.58	55.8	0.406	11.9
44	2.78	5.90	2.17	0.04	27.6	0.501	6.71
45	1.46	0.00	1.82	0.49	41.0	0.286	14.1
46	4.02	0.55	1.81	0.81	100.	0.207	20.3
47	3.78	16.69	1.82	0.25	100.	0.115	29.8
48	2.11	0.87	1.85	0.19	18.1	0.525	8.61
49	4.90	0.36	2.20*	0.33	72.5	0.211	19.6
50	4.51	0.00	2.20*	0.80	7.88	0.131	48.5
51	2.91	1.53	1.79	0.95	100.	0.112	45.2

Done, Davis, Blaes, Ward 2012

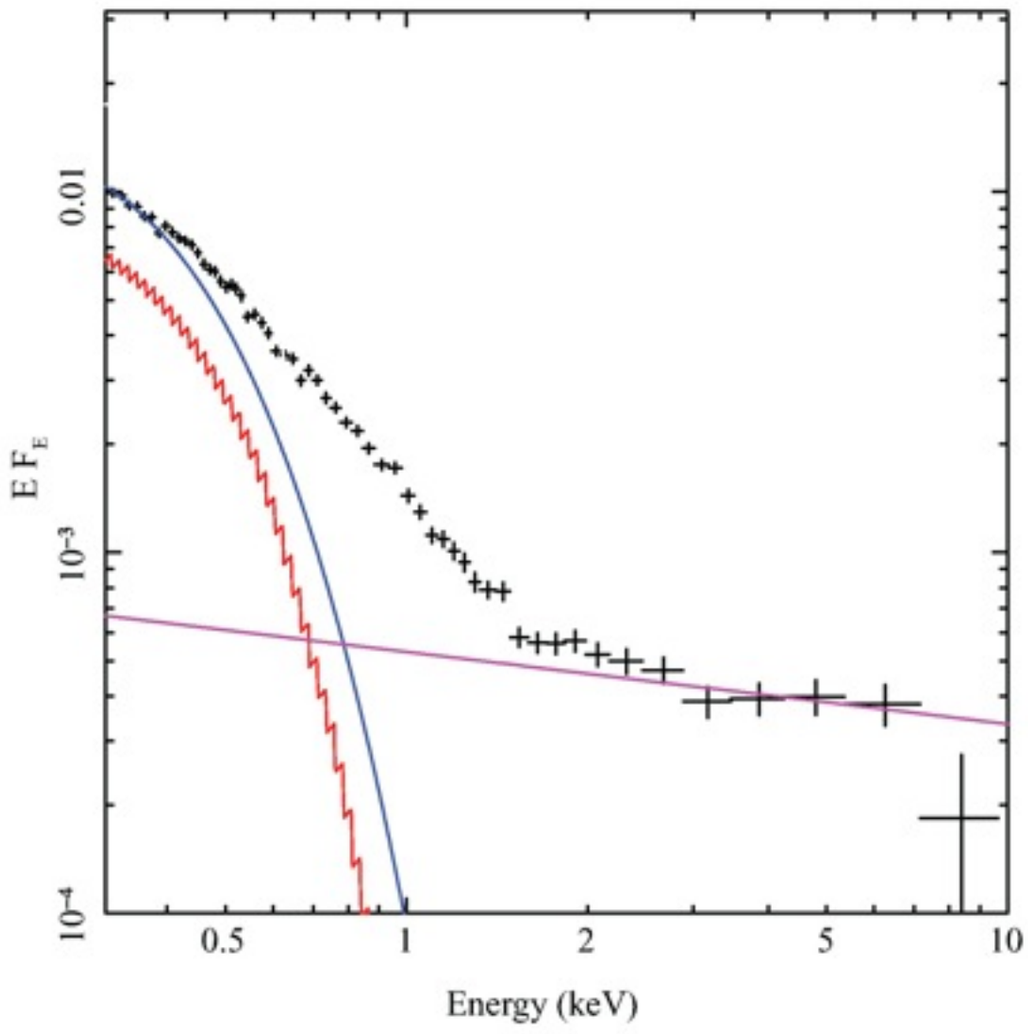

Figure 3. The *XMM–Newton* PN spectrum of RE J1034+396 (black points) compared to the full radiative transfer disc spectrum for $M = 10^6\,M_\odot$, $L/L_{Edd} = 1$ (red), together with the colour temperature corrected blackbody disc spectrum for $M = 10^6\,M_\odot$, $L/L_{Edd} = 1.15$ (blue). This can account for most of the 'soft X-ray excess' in this object, though the shape of the predicted disc spectrum is too steep to match the observed data in the 0.5–1 keV energy range even including the best-fitting 2–10 keV power law (magenta line).

Done, Davis, Blaes, Ward 2012

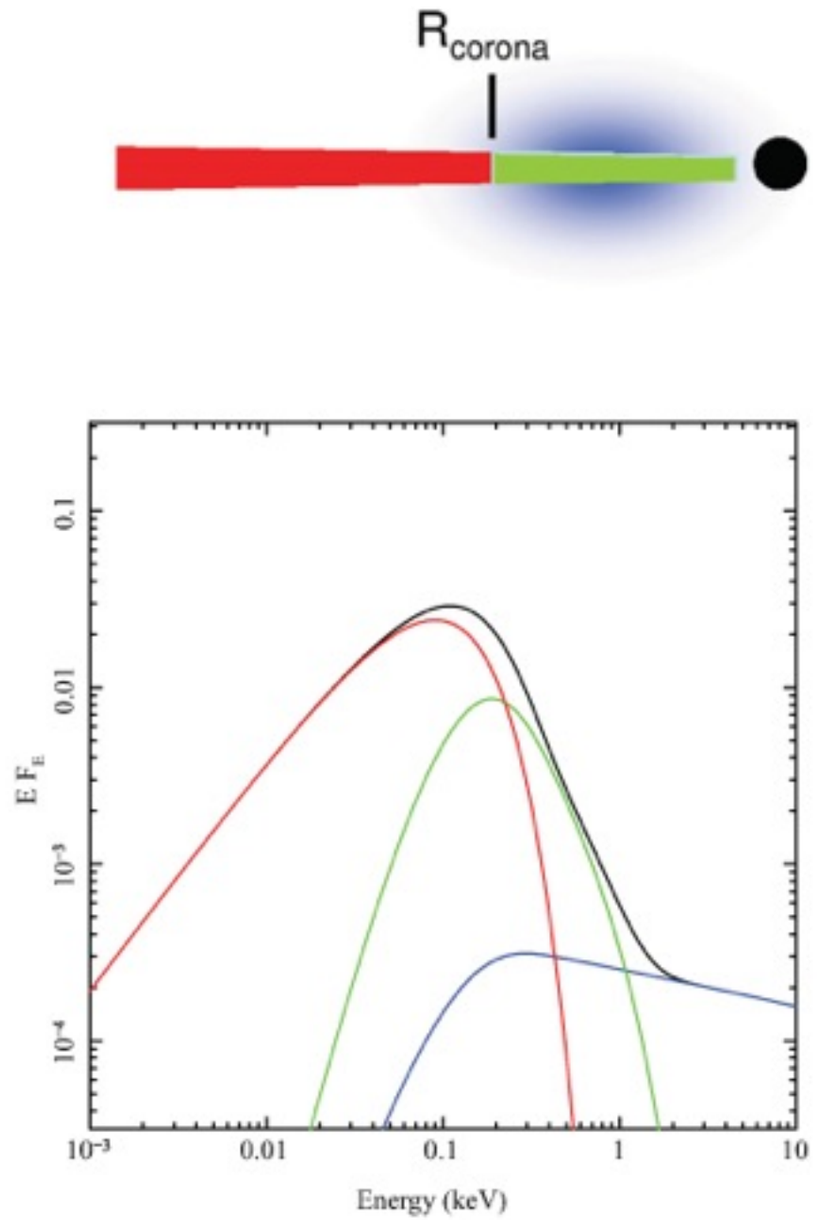

Figure 5. A schematic of the model geometry and resultant spectra, with outer disc (red) which emits as a (colour temperature corrected) black-body, and an inner disc (green) where the emission is instead Compton upscattered (perhaps by bulk turbulent motion in the disc, or by there being more dissipation in the effective photosphere than assumed in the standard Shakura–Sunyaev vertical dissipation profile). Some fraction of the energy is also Compton upscattered in a corona (blue) to produce the power-law tail to high energies.

Petrucci et al. 2013 , Mrk 509

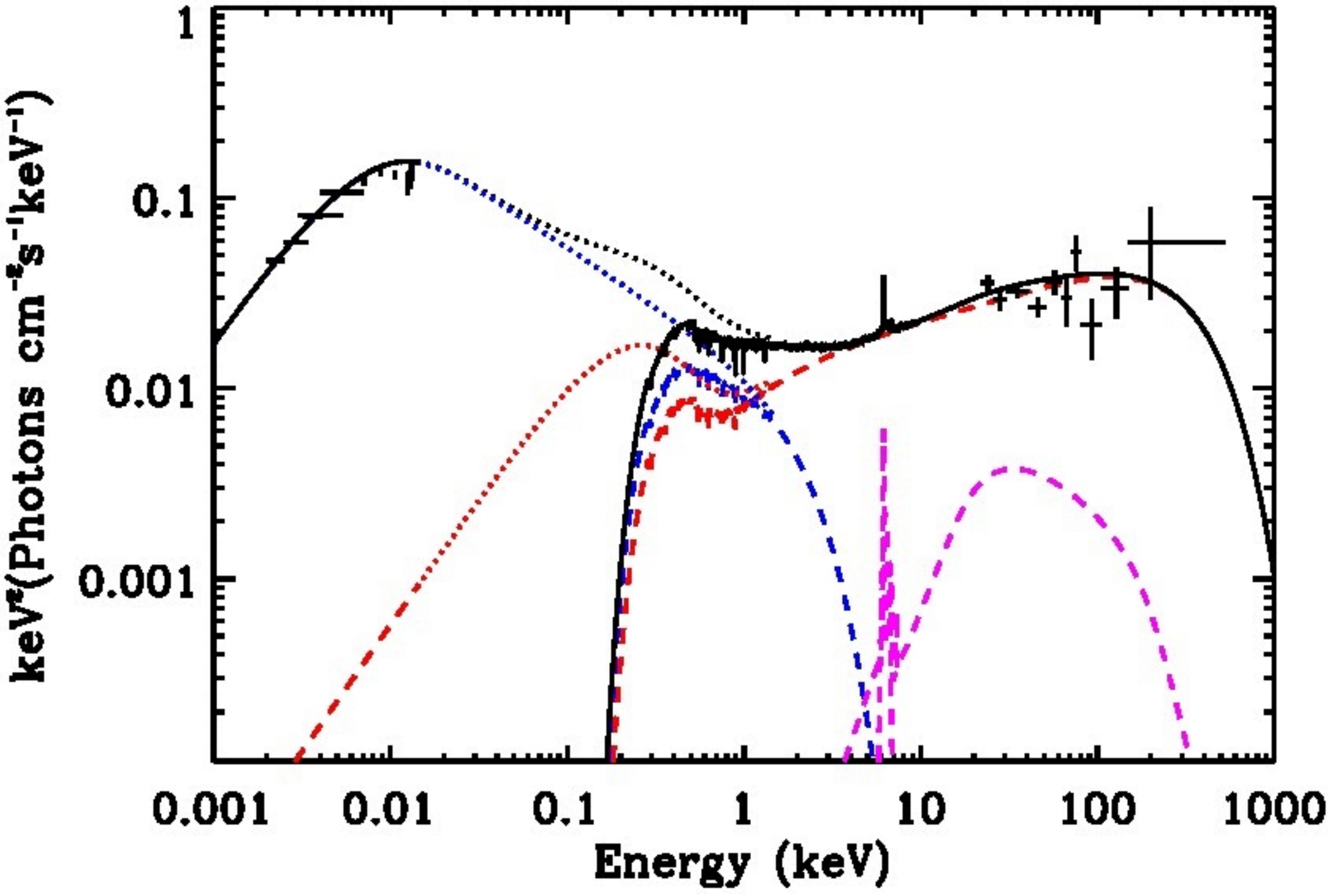

Petrucci et al. 2013, Mrk 509

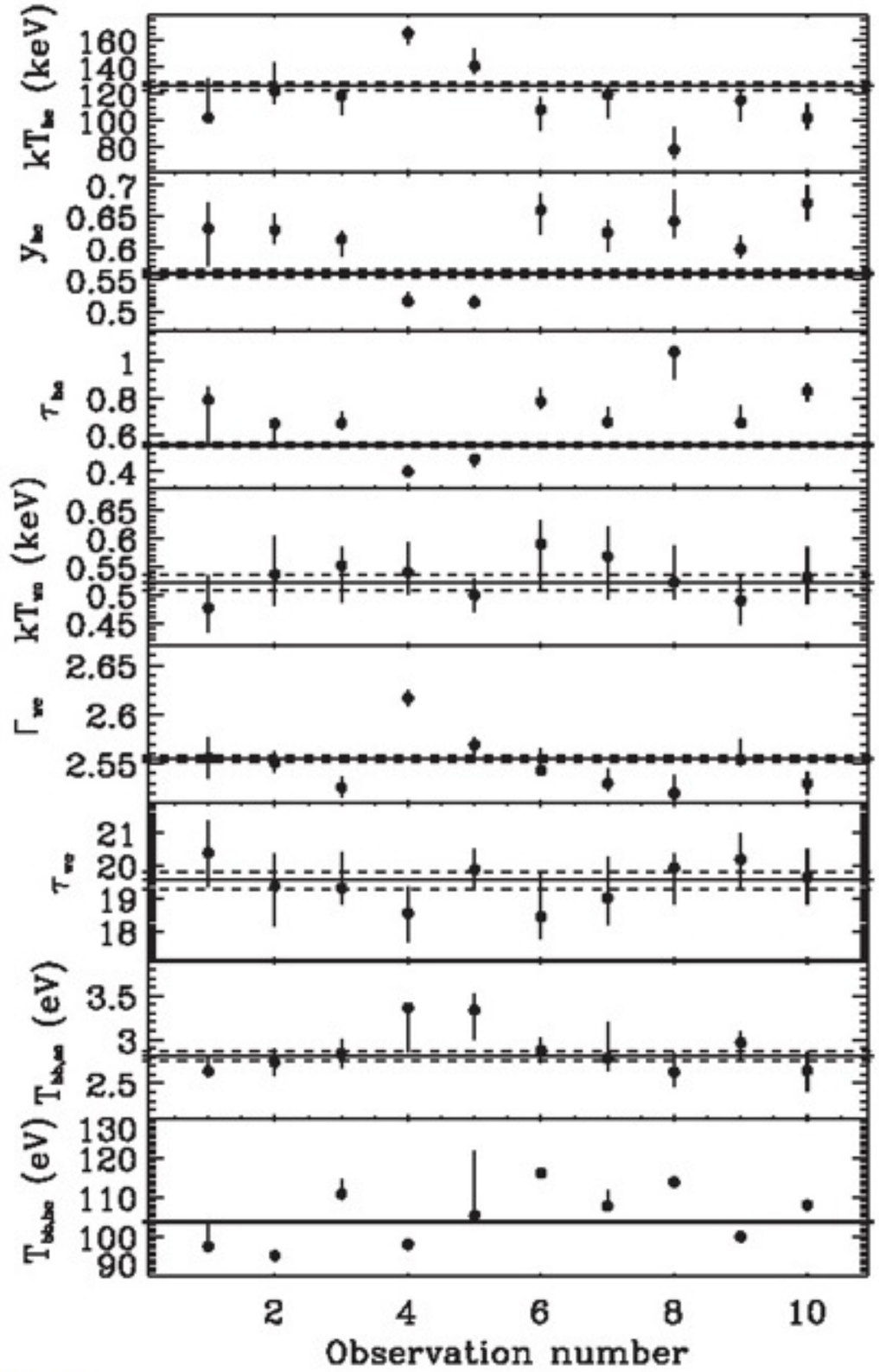

Fig. 7. Time evolution of the different fit parameters. From top to bottom: the HOT corona temperature kT_{hc}, Compton parameter y_{hc}, optical depth τ_{hc}, and the WARM corona temperature kT_{wc}, photon index Γ_{wc}, optical depth τ_{wc}, and the soft photon temperatures $T_{bb,wc}$ and $T_{bb,hc}$. The solid lines show the best-fit constant values and the solid lines the $\pm 1\sigma$ uncertainties.

Petrucci et al. 2013 , Mrk 509

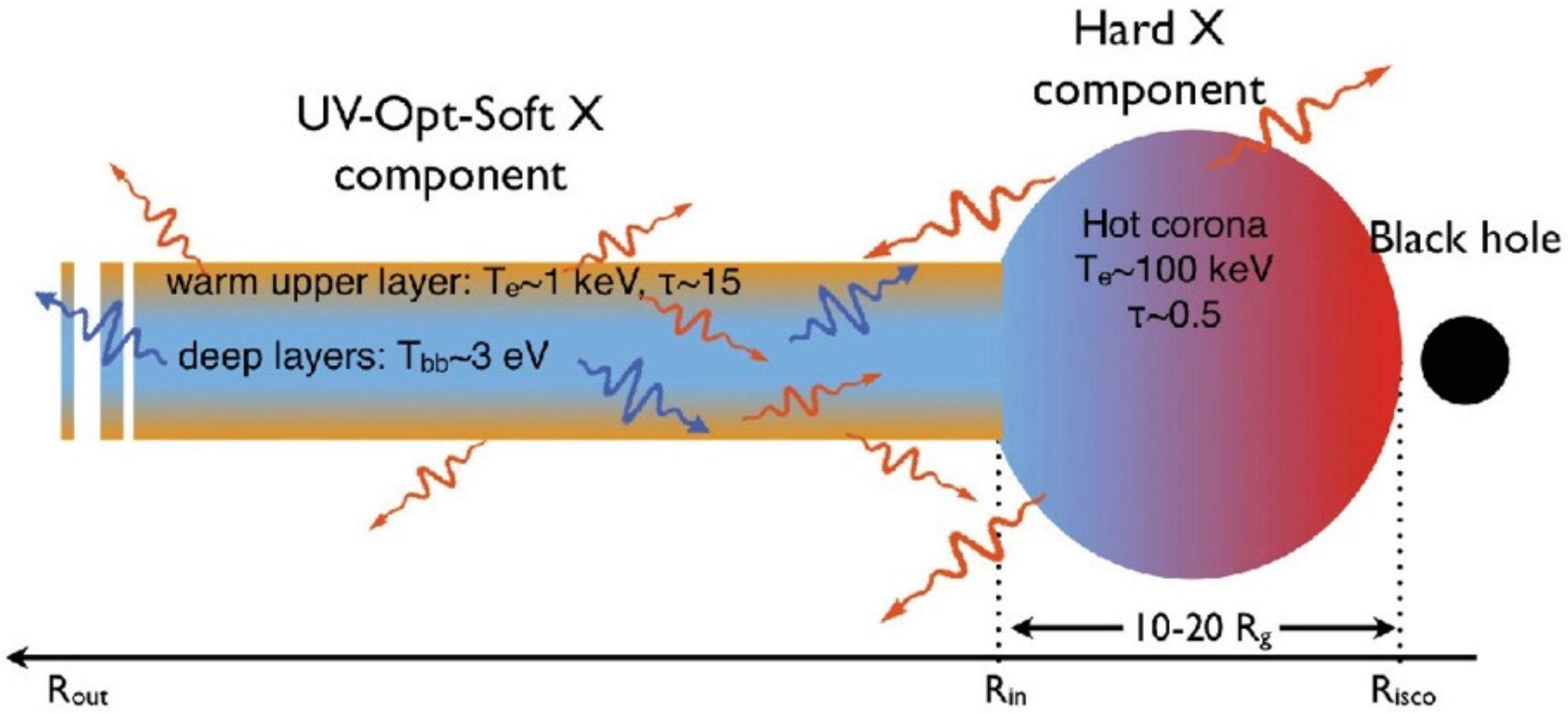

Fig. 10. A sketch of the accretion flow geometry in the inner region of the galaxy Mrk 509. The HOT corona, producing the hard X-ray emission, has a temperature of ~100 keV and optical depth ~0.5. It is localized in the inner part of the accretion flow ($R < R_{in}$) and illuminates the accretion disk beyond R_{in}, helping to form a WARM layer at the disk surface. This WARM component has a temperature of ~1 keV and an optical depth ~15 and produces the optical-UV up to soft X-ray emission. It extends over a large part of the accretion flow, heating the deeper layers and comptonizing their optical-UV emission. In return, part of this emission enters and cools the HOT corona.

Warm, **dissipated** corona, **optically thick**, cooled **purely by Compton scattering**

Warm, **dissipated** corona, **optically thick**, cooled **purely by Compton scattering**

1) $$\mu\frac{dI}{d\tau} = I - J - Q$$

purely scattered, dissipated corona

S=J+Q

Warm, **dissipated** corona, **optically thick**, cooled **purely by Compton scattering**

1) $$\mu\frac{dI}{d\tau} = I - J - Q$$

purely scattered, dissipated corona

S=J+Q

2) $$J(\tau) = 3H_{\rm disk}\left((\xi+1)\tau - \frac{\xi\tau^2}{2\tau_{\rm cor}} + \frac{2}{3}(\xi+1)\right)$$

Corona is cooled by **Compton scattering**

1) $$J(\tau)\frac{4kT_{\rm cor}}{m_{\rm e}c^2} = Q$$

Corona is cooled by **Compton scattering**

1) $$J(\tau)\frac{4kT_{\rm cor}}{m_{\rm e}c^2} = Q$$

2) $$T_{\rm cor}(\tau) = \frac{m_{\rm e}c^2 Q}{12kH_{\rm disk}}\left((\xi+1)\tau - \frac{\xi\tau^2}{2\tau_{\rm cor}} + \frac{2}{3}(\xi+1)\right)^{-1}$$

Corona is cooled by **Compton scattering**

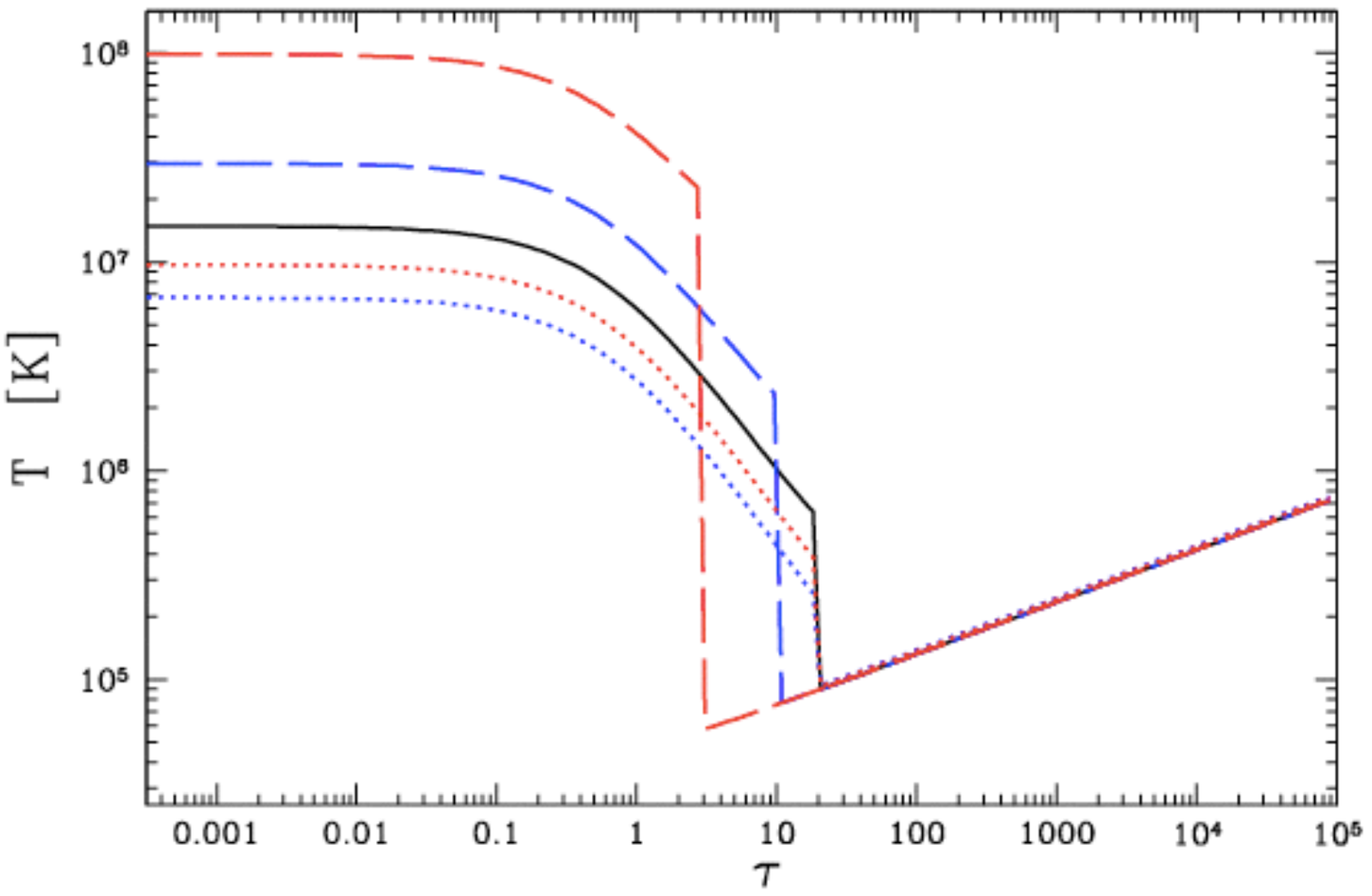

Fig. 1. The plot of the temperature vs. optical depth at 10 Schwarzschild radii from the black hole (see text for explanation). Integration was done up to $\tau_{tot} = 10^5$. Each curve represents the profile for following pairs of parameters ξ and τ_{cor}: 0.67 and 20 - black solid line, 0.67 and 3 - red dashed line, 0.67 and 10 - blue dashed line, 0.35 and 20 - red dotted line, and 0.22 and 20 - blue dotted line.

Corona in **hydrostatic equilibrium** with cold disc

1) $$\frac{dP_{\rm gas}}{d\tau} + \frac{dP_{\rm mag}}{d\tau} = \frac{1}{\kappa_{\rm es}} * \frac{GM_{\rm BH}}{R^3} * z - \frac{dP_{\rm rad}}{d\tau},$$

Corona in **hydrostatic equilibrium** with cold disc

1) $$\frac{dP_{\rm gas}}{d\tau} + \frac{dP_{\rm mag}}{d\tau} = \frac{1}{\kappa_{\rm es}} * \frac{GM_{\rm BH}}{R^3} * z - \frac{dP_{\rm rad}}{d\tau},$$

2) $$P_{\rm mag} = \frac{B^2_{\rm mag}}{8\pi} = \beta_{\rm m} P_{\rm gas}$$

3) $$P_{\rm rad} = \frac{4\pi}{c} H_{\rm disk} \left[\left(\tau + \frac{2}{3} \right) (\xi + 1) - \frac{\xi \tau^2}{2\tau_{\rm cor}} \right] ,$$

Corona in **hydrostatic equilibrium** with cold disc

1) $$\frac{dP_{\rm gas}}{d\tau} + \frac{dP_{\rm mag}}{d\tau} = \frac{1}{\kappa_{\rm es}} * \frac{GM_{\rm BH}}{R^3} * z - \frac{dP_{\rm rad}}{d\tau},$$

2) $$P_{\rm mag} = \frac{B_{\rm mag}^2}{8\pi} = \beta_{\rm m} P_{\rm gas}$$

3) $$P_{\rm rad} = \frac{4\pi}{c} H_{\rm disk} \left[\left(\tau + \frac{2}{3} \right) (\xi + 1) - \frac{\xi \tau^2}{2\tau_{\rm cor}} \right],$$

4) $$P_{\rm gas} = \frac{1}{(1+\beta_{\rm m})} \frac{4\pi}{c} H_{\rm disk} \left((\mathcal{G} - \xi - 1) * \tau + \frac{\xi \tau^2}{2\tau_{\rm cor}} \right)$$

Corona in **hydrostatic equilibrium** with cold disc

1) $$P_{\rm gas} = \frac{1}{(1+\beta_{\rm m})}\frac{4\pi}{c}H_{\rm disk}\left((\mathcal{G}-\xi-1)*\tau+\frac{\xi\tau^2}{2\tau_{\rm cor}}\right)$$

2) $$\rho = \frac{\mu m_{\rm H}}{kT}\frac{4\pi H_{\rm disk}}{c}*\left[(\mathcal{G}-\xi-1)*\tau+\frac{\xi\tau^2}{2\tau_{\rm cor}}\right]$$

Corona in **hydrostatic equilibrium** with cold disc

1) $$P_{\rm gas} = \frac{1}{(1+\beta_{\rm m})}\frac{4\pi}{c}H_{\rm disk}\left((\mathcal{G}-\xi-1)*\tau+\frac{\xi\tau^2}{2\tau_{\rm cor}}\right)$$

2) $$\rho = \frac{\mu m_{\rm H}}{kT}\frac{4\pi H_{\rm disk}}{c}*\left[(\mathcal{G}-\xi-1)*\tau+\frac{\xi\tau^2}{2\tau_{\rm cor}}\right]$$

3) $$\mathcal{G} = \frac{GM_{\rm BH}}{R^3}\frac{cZ_{\rm disk}}{4\pi\kappa_{\rm es}H_{\rm disk}}$$

4) $$\mathcal{G}-\xi-1=0$$

Corona in **hydrostatic equilibrium** with cold disc

1) $$P_{\rm gas} = \frac{1}{(1+\beta_{\rm m})}\frac{4\pi}{c}H_{\rm disk}\left((\mathcal{G}-\xi-1)*\tau+\frac{\xi\tau^2}{2\tau_{\rm cor}}\right)$$

2) $$\rho = \frac{\mu m_{\rm H}}{kT}\frac{4\pi H_{\rm disk}}{c}*\left[(\mathcal{G}-\xi-1)*\tau+\frac{\xi\tau^2}{2\tau_{\rm cor}}\right]$$

3) $$\mathcal{G} = \frac{GM_{\rm BH}}{R^3}\frac{cZ_{\rm disk}}{4\pi\kappa_{\rm es}H_{\rm disk}}$$

4) $$\mathcal{G}-\xi-1=0$$

Corona is **Compton dominated**

1) $$\frac{\Lambda_C}{\Lambda_B} = A(1+\beta_m)\frac{\xi^{1/2}}{\tau_{cor}^{1/2}\tau^2}\left[(\xi+1)\tau - \frac{\xi\tau^2}{2\tau_{cor}} + \frac{2}{3}(\xi+1)\right]^{-1/2}$$

Corona is **Compton dominated**

1) $$\frac{\Lambda_C}{\Lambda_B} = A(1+\beta_m)\frac{\xi^{1/2}}{\tau_{cor}^{1/2}\tau^2}\left[(\xi+1)\tau - \frac{\xi\tau^2}{2\tau_{cor}} + \frac{2}{3}(\xi+1)\right]^{-1/2}$$

2) $$\frac{\Lambda_C}{\Lambda_B} \cong A(1+\beta_m)\frac{\xi^{1/2}}{\tau_{cor}^{3}}\left(1+\frac{1}{2}\xi\right)^{-1/2}$$

at the base of the corona

The optical depth of the base of dissipated corona

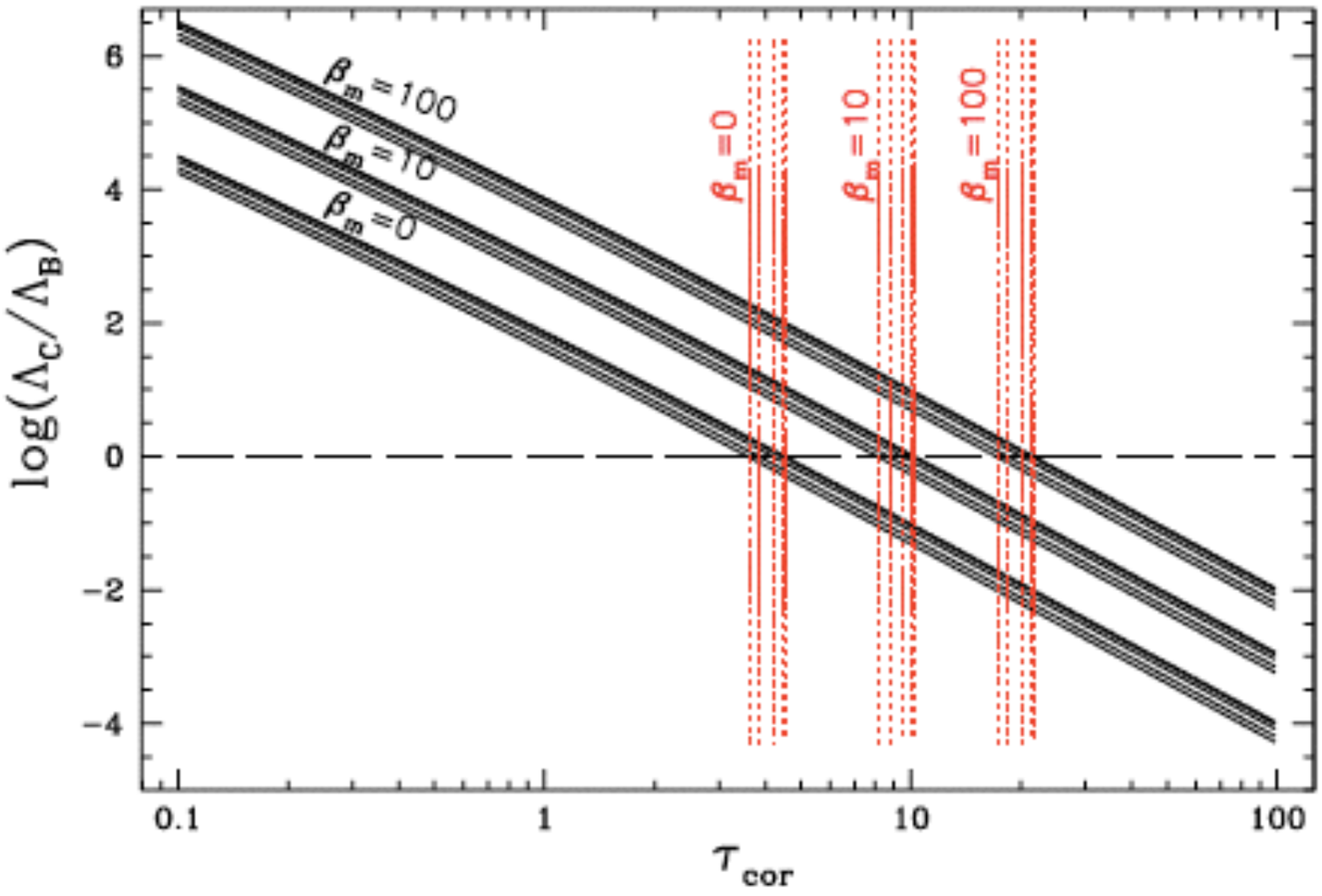

Fig. 2. The importance of Compton scattering over the bremsstrahlung at the base of corona for different values of τ_{cor} (Eq. 19). Solid lines in each package are computed for various values of $\xi = 0.22, 0.35, 0.67, 1.07$, and 1.33. Each package is calculated for three different values of magnetic pressure: $\beta_m = 0, 10$ and 100. Horizontal dashed line represents the case where $\Lambda_C/\Lambda_B = 1$, while vertical dotted liens mark values of coronal optical depth for which it happens.

Conclusions

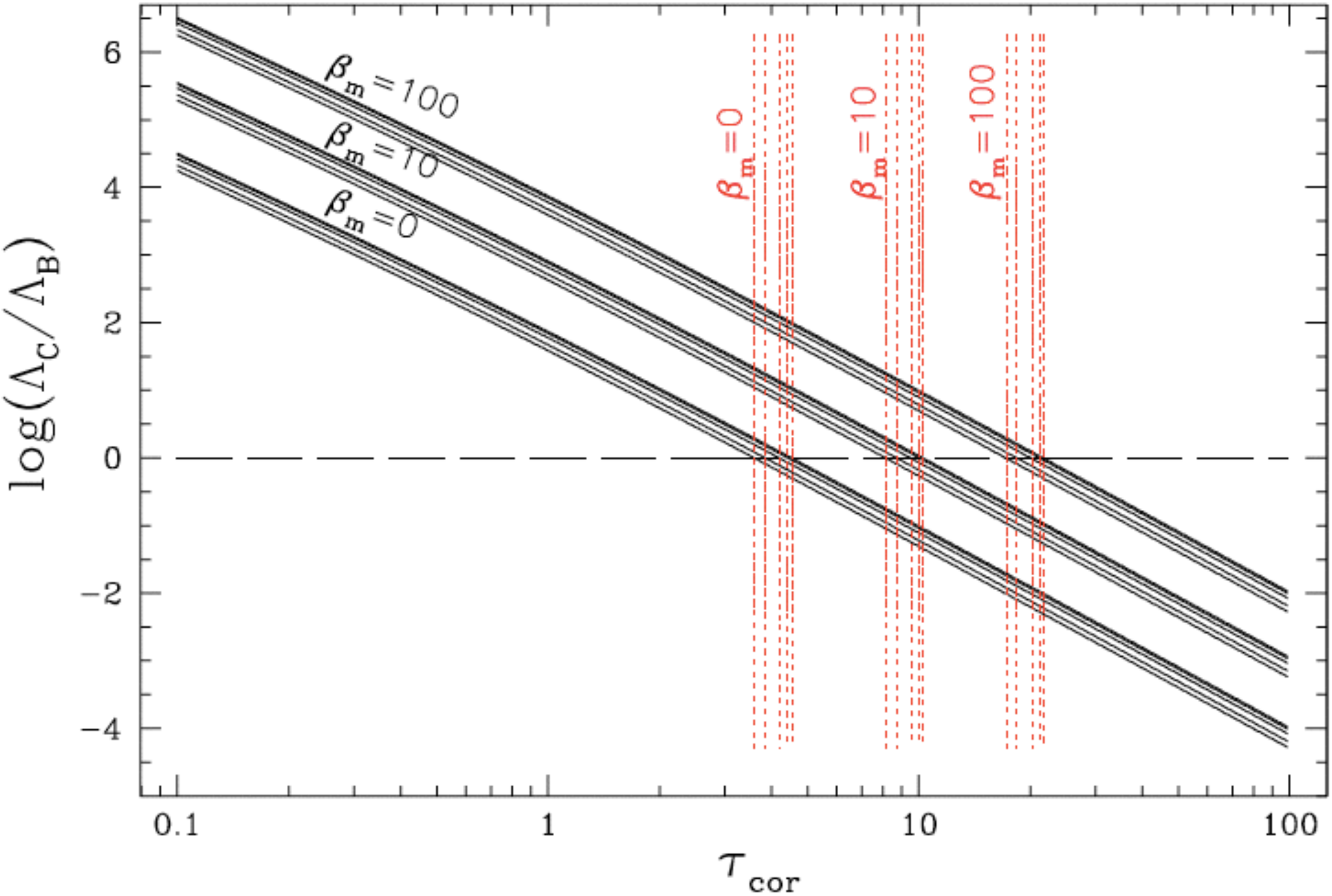

Conclusions

1) Dissipative corona purely cooled by Compton scattering heats up to ~ 1 keV on the base of radiative transfer.

2) Maximum optical depth of such corona:
optical depth in hydr. eq. ~ 4.5

3) The optical depth of soft corona is increasing when gas pressure is reduced for instance when magnetic pressure is increasing.

4) For $\beta_{\rm m} = 100$ **optical depth ~ 20** , but maybe there is another mechanism to low down the gas pressure ????

Vidok Restaurant , entrance from Zwierzyniecka str.